Forschungszentrum Karlsruhe
in der Helmholtz-Gemeinschaft

Wissenschaftliche Berichte
FZKA 6907

Problems in Fracture Mechanics of Indentation Cracks

T. Fett, G. Rizzi

Institut für Materialforschung

Oktober 2003

FORSCHUNGSZENTRUM KARLSRUHE

in der Helmholtz-Gemeinschaft

Wissenschaftliche Berichte

FZKA 6907

PROBLEMS IN FRACTURE MECHANICS OF INDENTATION CRACKS

T. Fett, G. Rizzi

Institut für Materialforschung

Forschungszentrum Karlsruhe GmbH, Karlsruhe

2003

Impressum der Print-Ausgabe:

Als Manuskript gedruckt

Forschungszentrum Karlsruhe GmbH
Postfach 3640, 76021 Karlsruhe

Mitglied der Hermann von Helmholtz-Gemeinschaft
Deutscher Forschungszentren (HGF)

ISSN 0947-8620

Problems in fracture mechanics of indentation cracks

Abstract:

Vickers indentation cracks are an appropriate tool to determine the crack-tip toughness K_{I0} of ceramics from the total crack opening displacements. Two different procedures were applied to determine the crack opening displacement (COD) field under residual and externally applied stress fields. First, a semi-analytical procedure was used to compute the COD field from residual stresses introduced in the uncracked body by the indentation test. This approach allows a description by analytical relations. In order to check the accuracy of these calculations and to outline some problems in detail, also finite element (FE) computations were carried out. In an experimental example the stress intensity factor of glass is determined. Apart from the crack opening profile, also relations for the total stress intensity factor and the T-stress term are provided.

As a second type of indentation crack, cone cracks were considered as developing under spherical contact load. Mixed-mode stress intensity factors were computed. The results obtained by application of the weight function method are used to calculate the cone angle under the condition of K_{II}=0 during crack generation. A good agreement with measured data from literature is found.

Probleme in der bruchmechanischen Behandlung von Eindrucksrissen

Kurzfassung:

Die beim Vickers-Eindruckversuch in keramischen Materialien auftretenden Risse sind geeignet, die Rissspitzenzähigkeit K_{I0} von Keramiken aus Rissuferverschiebungsmessungen zu bestimmen. Es werden zwei verschiedene Methoden verwendet, um die Rissuferverschiebung unter Eigenspannungsbelastung durch den Eindruck selbst und zusätzlich aufgrund von extern aufgebrachten Belastungen zu berechnen. Zuerst wird eine halbanalytische Vorgehensweise dargestellt. Diese ist besonders geeignet, um analytische Beziehungen zwischen Rissuferverschiebung und aktuell herrschendem Spannungsintensitätsfaktor zu beschreiben. Zusätzlich wird eine Analyse mit der Methode der Finiten Elemente durchgeführt, die es gestattet, Detailprobleme, wie z.B. die Ermittlung der T-Spannung, zu behandeln.

Als zweiter Eindrucksriss-Typ wird der „cone crack“ behandelt. Hierbei wird die Gewichtsfunktion – einschließlich gemischter Terme – ermittelt und mit deren Hilfe der Rissausbreitungswinkel aus der Bedingung des verschwindenden mode-II Spannungsintensitätsfaktors bestimmt. Eine sehr gute Übereinstimmung mit Messdaten wird gefunden.

Contents

VICKERS INDENTATION CRACKS

I SEMI-ANALYTICAL STUDY

1. Crack shape 1

2. Crack opening in the absence of externally applied loads 3

2.1 Residual stresses 3

2.2 Residual stress intensity factor 4

2.3 Displacements caused by the residual stresses 5

2.4 Contact stresses, contact stress intensity factor and related COD 7

2.5 Total stress intensity factor and total COD 9

3. Superposition of external stresses 12

3.1 Applied stress intensity factor and displacement 12

3.2 Impacts of variable contact stresses on crack extension under an externally applied load 15

4 Determination of *K* from the COD profile 18

II FINITE ELEMENT STUDY

5. Stress intensity factor and T-stress 19

5.1 Importance of T-stress 19

5.2 Penny-shaped crack in an infinite body under remote tension 20

5.3 Penny-shaped crack under crack-face loading 21

5.4 Penny-shaped crack under superimposed internal stresses and remote tension 25

III SUMMARY OF RESULTS FOR VICKERS CRACKS

Loading by residual stress field 27

Loading by superimposed externally applied stresses 28

CONE CRACKS

6. Cone crack formation 29

7. Weight functions 30

7.1 Weight function procedure 30

7.2 Weight function from FE computations 31

8. Application of the weight functions to cone crack problems 36

8.1 Hertzian contact stresses 36

8.2 Stresses under a flat stamp 37

8.3 Principal effect of a rising crack growth resistance 38

8.4 T-stresses for line loads 39

8.5 Stress intensity factors and T-stress under Hertzian contact load 44

References 46

VICKERS INDENTATION CRACKS

I SEMI-ANALYTICAL STUDY

1. Crack shape

Vickers indentation cracks are an appropriate tool to determine the crack tip toughness K_{I0} from the total crack opening displacements. In a preceding study [1] two contributions to the total crack opening displacement field were addressed. First, the residual stresses occurring in the uncracked body were considered and then, the contact stresses generated by preventing crack-face penetration were computed. Treatment of these displacement fields is sufficient for the description of a Vickers indentation crack in the absence of externally applied loads. Very often, the behaviour of such cracks is investigated under additionally applied loads. The present report is aimed at computing the total crack opening displacement field caused by a superposition of residual stresses in the uncracked material, which result from Vickers indentation, contact stresses in the inner contact zone, and externally applied stresses.

For these considerations, the indentation crack is assumed to be semi-circular (Fig. 1). It is furthermore assumed that the crack can be described by half of a fully embedded crack, i.e. a change of the stress intensity factor along the crack contour is neglected.

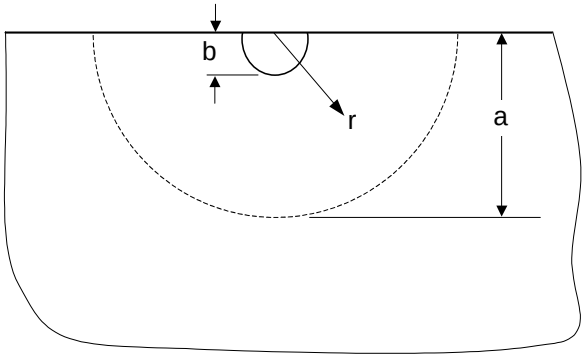

Fig. 1 Vickers indentation crack (geometrical parameters).

In a fracture mechanics treatment of the crack problem, we first have to decide on which type of crack is present. Fractured test specimens with Vickers indentation cracks mostly allow the crack tip contour at $r=a$ (Fig. 1) to be observed. The inner boundary of the open crack can be derived from the COD profile observable on the specimen surface (Fig. 2).

Microscopic observations reveal two possible crack types:

- A semi-circular crack of radius a, which is closed in the inner region $r \leq d \approx b$ (Fig. 3a).
- A ring-shaped crack of outer radius a and inner radius d (Fig. 3b).

In Fig. 3 the possible cracks are shaded. The type of crack can be determined easily by the use of the Irwin relation that relates the crack opening displacement δ to the stress intensity factor *K*. In the case of a ring-shaped crack, two stress singularities and two stress intensity factors must occur, namely, one at the inner crack contour (*r*=*d*) and one at the outer contour (*r*=*a*). Directly after crack generation, the stress intensity factor at the outer contour equals fracture toughness K_{Ic}. The related COD is given as

$$\delta_{r\to a} = \sqrt{\frac{8}{\pi}}\,\frac{K_{Ic}}{E'}\sqrt{a-r} \tag{1}$$

with the effective Young's modulus *E'* denoting

$$E' = \begin{cases} E & \text{plane stress} \\ E/(1-\nu^2) & \text{plane strain} \end{cases} \tag{2}$$

(*E*=Young's modulus, ν=Poisson's ratio).

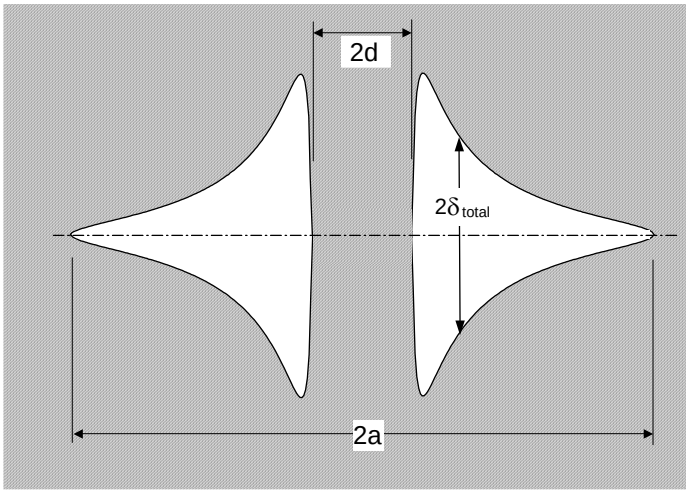

Fig. 2 Crack opening profile on the specimen surface (schematic representation).

From microscopic observation, it is well known that at the same distance from the crack tip the crack opening displacement at the inner crack contour by far exceeds that at the outer contour

$$\delta\big|_{d+\varepsilon} >> \delta\big|_{a-\varepsilon} \quad , \qquad \varepsilon << a, d \tag{3}$$

In the case of a ring crack, the stress intensity factor at the inner crack tip must be much larger than K_{Ic}, and this is impossible. Consequently, it may be concluded that the crack observed must be a semi-circular crack.

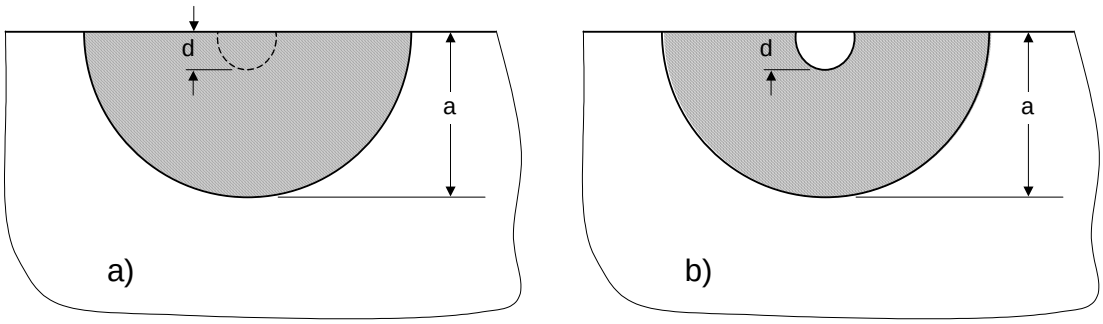

Fig. 3 Possible crack types to be concluded from microscopic observation, a) semi-circular surface crack, b) half of a ring crack.

2. Crack opening in the absence of externally applied loads

2.1 Residual stresses

Beneath the contact area of an indenter pressed into the surface of a brittle material, a residual stress zone remains after unloading (Fig. 4a). As an approximation of the residual stress field in the uncracked body, the model of an internally pressurised cavity in an infinite body [2] may be applied [3, 4]. This model yields the tangential component of residual stresses

$$\sigma_{res} = \begin{cases} -p_0 & \text{for } r < b \\ \frac{1}{2} p_0 (b/r)^3 & \text{for } r > b \end{cases} \tag{4a}$$

as plotted in Fig. 4b. Residual stresses caused by a Vickers indentation may be modified due to the occurrence of a free surface. Since the stress component normal to the surface must vanish, the residual stresses decrease at the surface. This is indicated by the dashed curve in Fig. 4c. If the stresses in $r<b$ are considered to be variable with r, i.e. $\sigma=\sigma(r/b)$, the principle of Saint Venant ensures (at least at a distance comparable to b) that the stresses outside correspond to that resulting from a constant inner stress $p \le p_0$, which is identical with the average stress in $r<b$. This approximation is indicated by the solid curve in Fig. 4c. Consequently, it can be written that

$$\sigma_{res} = \begin{cases} -p\, f(r/b) & \text{for } r < b \\ C\, p\, (b/r)^3 & \text{for } r > b \end{cases} \tag{4b}$$

with the coefficient C resulting from the equilibrium condition as

$$C = \frac{1}{b^2} \int_0^b f(r/b)\, r\, dr \tag{5}$$

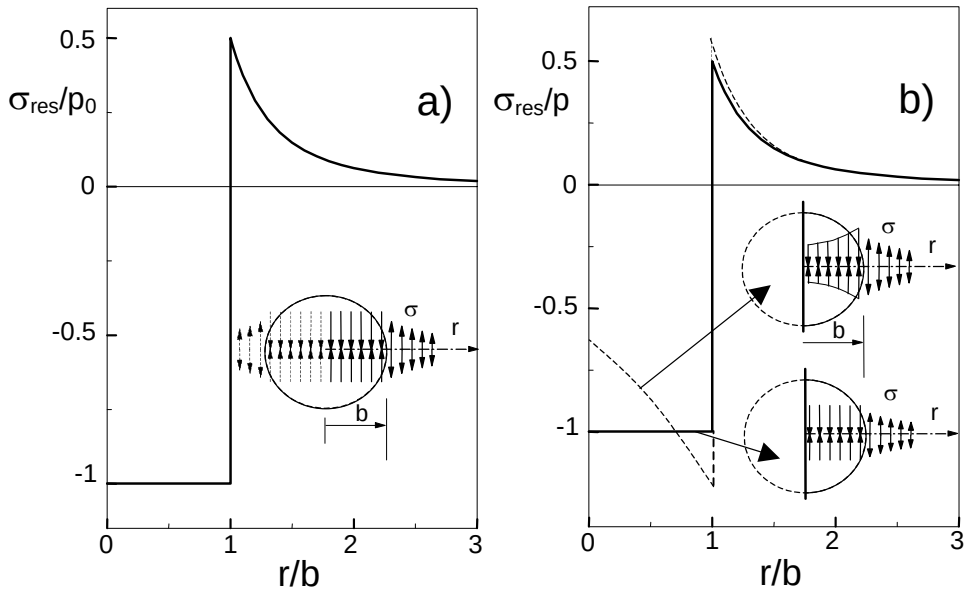

Fig. 4 a) Residual stresses in the uncracked body for a cavity in an infinite body, b) residual stresses in the presence of a free surface (semi-infinite body).

The residual stresses cause of the crack opening behaviour of Vickers indentation cracks illustrated in Fig. 2.

2.2 Residual stress intensity factor

The residual stress intensity factor of a crack of radius a is given as

$$K_{res} = \frac{2}{\sqrt{\pi a}} \int_0^a \frac{r \sigma_{res}(r)\, dr}{\sqrt{a^2 - r^2}} \tag{6a}$$

or

$$K_{res} = -\frac{2}{\sqrt{\pi a}} \int_0^b \frac{r\ p\ f(r/b)\, dr}{\sqrt{a^2 - r^2}} + \frac{2C\,p}{\sqrt{\pi a}} \left(\frac{b}{a}\right)^2 \sqrt{a^2 - b^2} \tag{6b}$$

As outlined in [1], it can be shown that the residual stress intensity factor is negative for any function $f(r/b)$ and any crack size a. Application of the mean value theorem to the first term of eq.(6b) and use of eq.(5) yield

$$-\frac{2}{\sqrt{\pi a}} \int_0^b \frac{r\ p\ f(r/b)\, dr}{\sqrt{a^2 - r^2}} = -\frac{2p}{\sqrt{\pi a}} \frac{1}{\sqrt{a^2 - r_0^2}} \int_0^b r\ f(r/b)\, dr \xrightarrow{eq.(2)} = -\frac{2C\,p}{\sqrt{\pi a}} \frac{b^2}{\sqrt{a^2 - r_0^2}}$$

with a certain radius $0 \le r_0 \le b$.

$$K_{res} = -\frac{2C\,p b^2}{a^{3/2}\sqrt{\pi}} \left(\frac{1}{\sqrt{1 - (r_0/a)^2}} - \sqrt{1 - (b/a)^2} \right) \le 0 \tag{7}$$

since the bracket is positive for any r_0 and b. As a first consequence of the negative residual stress intensity factor, penetration of the crack faces has to be expected for the near-tip crack opening displacement field at least.

All further considerations concentrate on the case of $f(r/b)=1$, i.e. constant pressure distribution in the uncracked body, as originally proposed by Hill [2]. In this case, the residual stress intensity factor is given as

$$K_{res} = -\frac{2p}{\sqrt{\pi a}}\left(a - \sqrt{a^2 - b^2}\right) + \frac{p}{\sqrt{\pi a}}\left(\frac{b}{a}\right)^2 \sqrt{a^2 - b^2} \tag{8}$$

Figure 5 shows the residual stress intensity factor K'_{res} in the normalisation of

$$K' = \frac{K}{p\sqrt{b}} \tag{9}$$

as the circles. The straight line which excellently fits to the circles in the range of $3<a/b<6$ can be expressed by

$$K'_{res} \cong -0.4707\,(b/a)^{3.56} \tag{10}$$

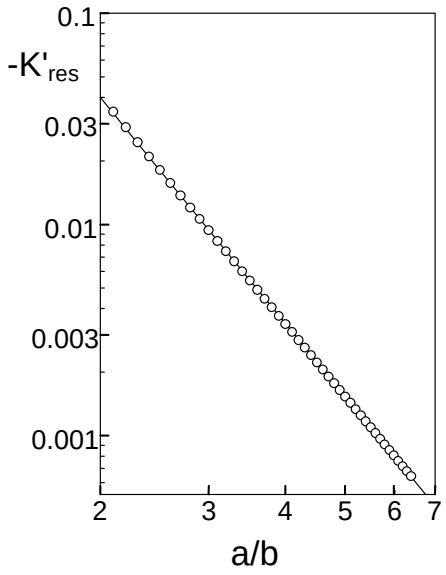

Fig. 5 Residual stress intensity factor K'_{res} normalised according to eq.(9); circles: eq.(8), straight line: eq.(10).

2.3 Displacements caused by the residual stresses

In order to demonstrate the penetration of crack faces in the residual stress field, the crack opening displacements δ have to be computed. It holds that

$$\delta_{res}(r) = \frac{4}{\pi E'}\int_r^a \left(\int_0^{a'} \frac{r'\sigma_{res}(r')}{\sqrt{a'^2 - r'^2}}\,dr' \right) \frac{da'}{\sqrt{a'^2 - r^2}} \tag{11}$$

with the Young's modulus for plane strain E'. For a simpler representation of results, the crack opening displacements are normalised as

$$\delta' = \frac{\pi E'}{4pb}\delta \tag{12}$$

Figure 6 shows the crack opening displacements δ_{res}. The displacements (Figs. 6a and 6b) are negative over the whole crack area and crack face penetration occurs at any distance r/a.

The residual displacements δ_1 caused by the stresses at $r/b < 1$ are [1]

$$\delta = \delta_1 + \delta_2$$

$$\delta_1 = -\frac{4ap}{\pi E'}\left[\sqrt{1-\left(\frac{r}{a}\right)^2}\left(1-\sqrt{1-\left(\frac{b}{a}\right)^2}\right) + \frac{b}{a}\left[\mathbf{E}\left(\left(\frac{r}{b}\right)^2\right) - E\left(\arcsin\left(\frac{b}{a}\right), \left(\frac{r}{b}\right)^2\right)\right]\right], \quad r < b \tag{13a}$$

$$\begin{aligned}\delta_1 = -\frac{4ap}{\pi E'}\Bigg[&\sqrt{1-\left(\frac{r}{a}\right)^2}\left(1-\sqrt{1-\left(\frac{b}{a}\right)^2}\right) + \frac{r}{a}\left[\mathbf{E}\left(\left(\frac{b}{r}\right)^2\right) - E\left(\arcsin\frac{r}{a}, \left(\frac{b}{r}\right)^2\right)\right.\\ &\left.\left. - \left(1-\left(\frac{b}{r}\right)^2\right)\left(\mathbf{K}\left(\left(\frac{b}{r}\right)^2\right) - F\ \left(\arcsin\frac{r}{a}, \left(\frac{b}{r}\right)^2\right)\right)\right]\Bigg], \quad r > b\end{aligned} \tag{13b}$$

$$\delta_2 = \frac{2bp}{\pi E'}\frac{b}{r}\left[E\left(\arcsin\left(\frac{r}{b}, \left(\frac{b}{r}\right)^2\right) - E\left(\arcsin\left(\frac{r}{a}, \left(\frac{b}{r}\right)^2\right)\right], \quad r < b\right. \tag{14a}$$

$$\delta_2 = \frac{2bp}{\pi E'}\frac{b}{r}\left[\mathbf{E}\left(\left(\frac{b}{r}\right)^2\right) - E\left(\arcsin\left(\frac{r}{a}, \left(\frac{b}{r}\right)^2\right)\right], \quad r > b\right. \tag{14b}$$

with the complete elliptical integrals of the first and second kind **K** and **E** and the incomplete elliptical integrals E and F.

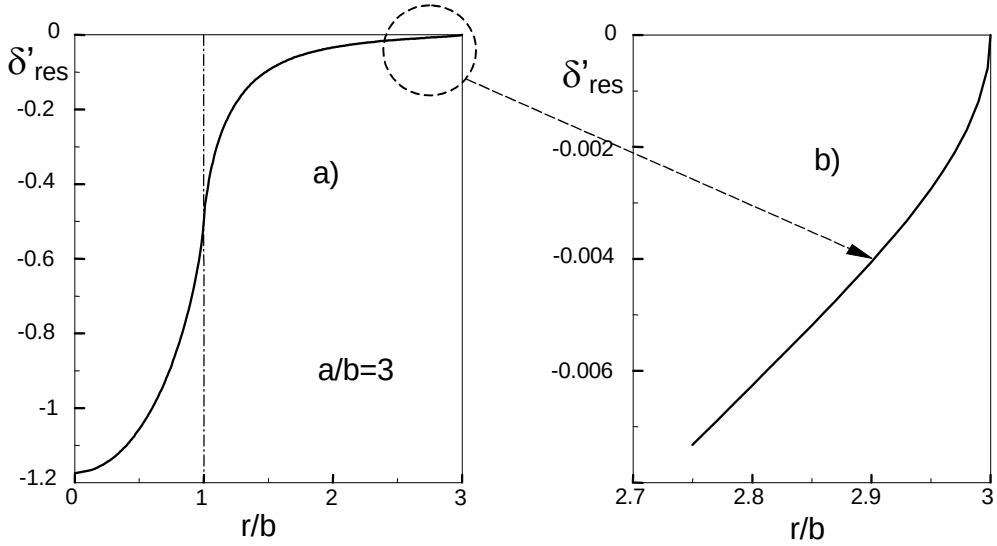

Fig. 6 Residual COD of a crack, a), b) crack opening displacements.

2.4 Contact stresses, contact stress intensity factor, and related COD

In a real structure crack penetration is not possible, of course. Prevented crack face penetration results in a distribution of (positive) contact stresses σ_{cont} which cause a positive contact COD field δ_{cont}

$$\delta_{cont}(r) = \frac{4}{\pi E'} \int_r^a \left(\int_0^{a'} \frac{r' \sigma_{cont}(r')}{\sqrt{a'^2 - r'^2}} dr' \right) \frac{da'}{\sqrt{a'^2 - r^2}} \tag{15}$$

and a contact stress intensity factor

$$K_{cont} = \frac{2}{\sqrt{\pi a}} \int_0^a \frac{r \sigma_{cont}(r)\, dr}{\sqrt{a^2 - r^2}} \tag{16}$$

This stress intensity factor is positive, since the contact stresses open the crack. The related contact stresses are restricted to a contact area of radius d with $d \cong b$ and must disappear in the region of real (positive) crack opening (see Fig. 7). To determine the contact stresses, the ***mixed boundary value problem*** has to be solved

$$\begin{aligned} \delta_{total} &= \delta_{res} + \delta_{cont} = 0 \quad \text{for} \quad r \le d \\ \sigma_{cont} &= 0 \qquad\qquad\qquad\quad \text{for} \quad r > d \end{aligned} \tag{17a}$$

or, explicitly,

$$\begin{aligned} \frac{4}{\pi E'} \int_r^a \left(\int_0^{a'} \frac{r' [\sigma_{res}(r') + \sigma_{cont}(r')]}{\sqrt{a'^2 - r'^2}} dr' \right) \frac{da'}{\sqrt{a'^2 - r^2}} &= 0 \qquad \text{for} \quad r \le d \\ \sigma_{cont} &= 0 \qquad\qquad\qquad\quad \text{for} \quad r > d \end{aligned} \tag{17b}$$

A numerical solution of eq.(17) was given in [1]. For the numerical treatment, a power series expansion (truncated after the term N) of the unknown contact stresses is applied according to

$$\sigma_{cont} = \begin{cases} \sum_{n=0}^{N} A_n r'^n & for \quad r' \le d \\ 0 & else \end{cases} \tag{18}$$

The unknown coefficients A_n can determined exclusively from the condition of $\delta_{total} = 0$ for $r < d$. Computations were performed for different values of d. It was found in [1] that for the contact displacement field at $r > \max(d,b)$ no significant influence of d was detectable. Therefore, further considerations were restricted to

$$d \cong b\,.$$

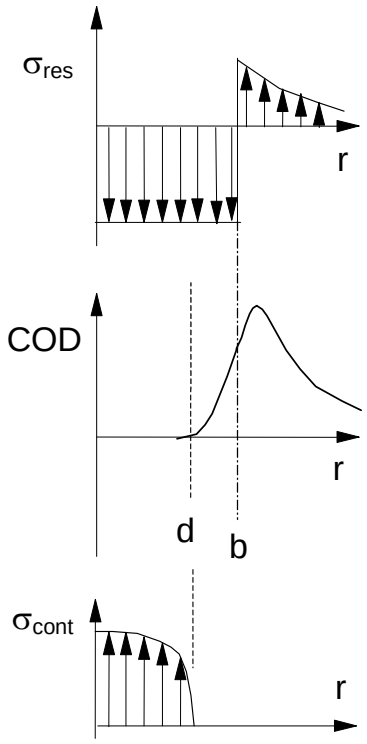

Fig. 7 Contact stresses in the centre region of a Vickers crack.

The numerically determined contact stresses could be adequately expressed by [1]

$$\sigma_{cont} = D_0(1-(r/b)^{q_0})p \tag{19a}$$

where the subscript "0" of the parameters D_0 and q_0 indicates the absence of an externally applied load. The parameters D_0 and q_0 may be approximated by

$$D_0 \cong 0.898 + 0.1127\,b/a \tag{19b}$$

$$q_0 \cong 5.32 + 2.69\,b/a + 13.33(b/a)^2 \tag{19c}$$

2.5 Total stress intensity factor and total COD

The really active total stress intensity factor is then

$$K_{total} = K_{res} + K_{cont} \tag{20}$$

and the total crack opening displacements are given by

$$\delta_{total}(r) = \frac{4}{\pi E'} \int_r^a \left(\int_0^{a'} \frac{r' \sigma_{total}(r')}{\sqrt{a'^2 - r'^2}} dr' \right) \frac{da'}{\sqrt{a'^2 - r^2}} \tag{21}$$

with the total stress

$$\sigma_{total} = \sigma_{res} + \sigma_{cont} \tag{22}$$

The total displacements δ_{total} were found by the superposition of the two solutions for δ_{res} and δ_{cont} (Figs. 8a, 8b).

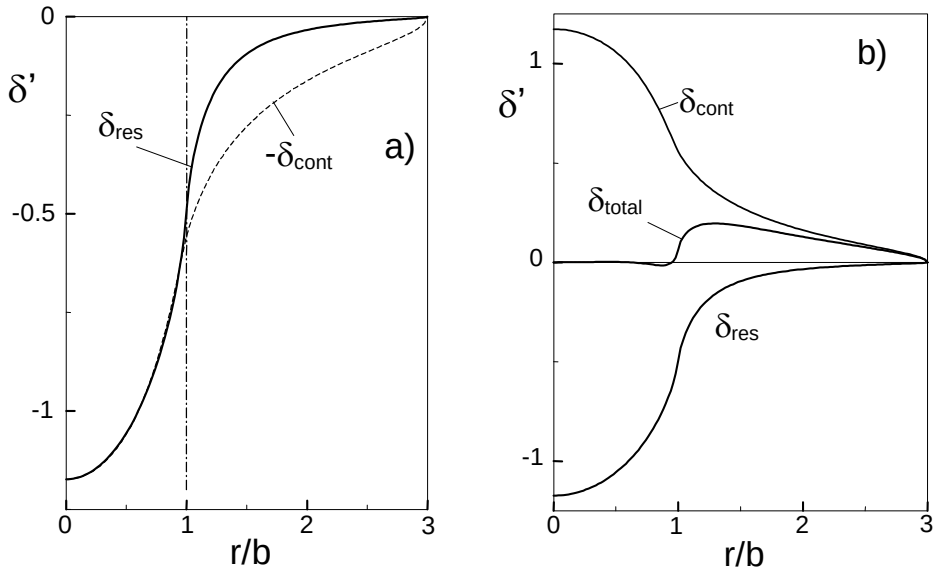

Fig. 8 a) Fitting of the displacements in $0<r<b$, b) total displacements δ_{total} obtained by superposition of residual and contact displacements.

The small deviations from $\delta_{total} = 0$ in $0 \le r \le b$ indicate the slight differences between the correct and the approximate contact stress solutions.

Total displacements are represented in Fig. 9a for several relative crack lengths a/b. The corresponding (normalised) total stress intensity factor is plotted in Fig. 9b, exhibiting the well-established proportionality $K \propto a^{-3/2}$ for $a/b \ge 2.5$

$$K'_{total} \cong \frac{0.372}{(a/b)^{3/2}} \tag{23}$$

Relation (23) allows to estimate the pressure p from the experimentally determined dependency between indentation load P and crack size

$$K = \chi \frac{P}{a^{3/2}} \tag{24}$$

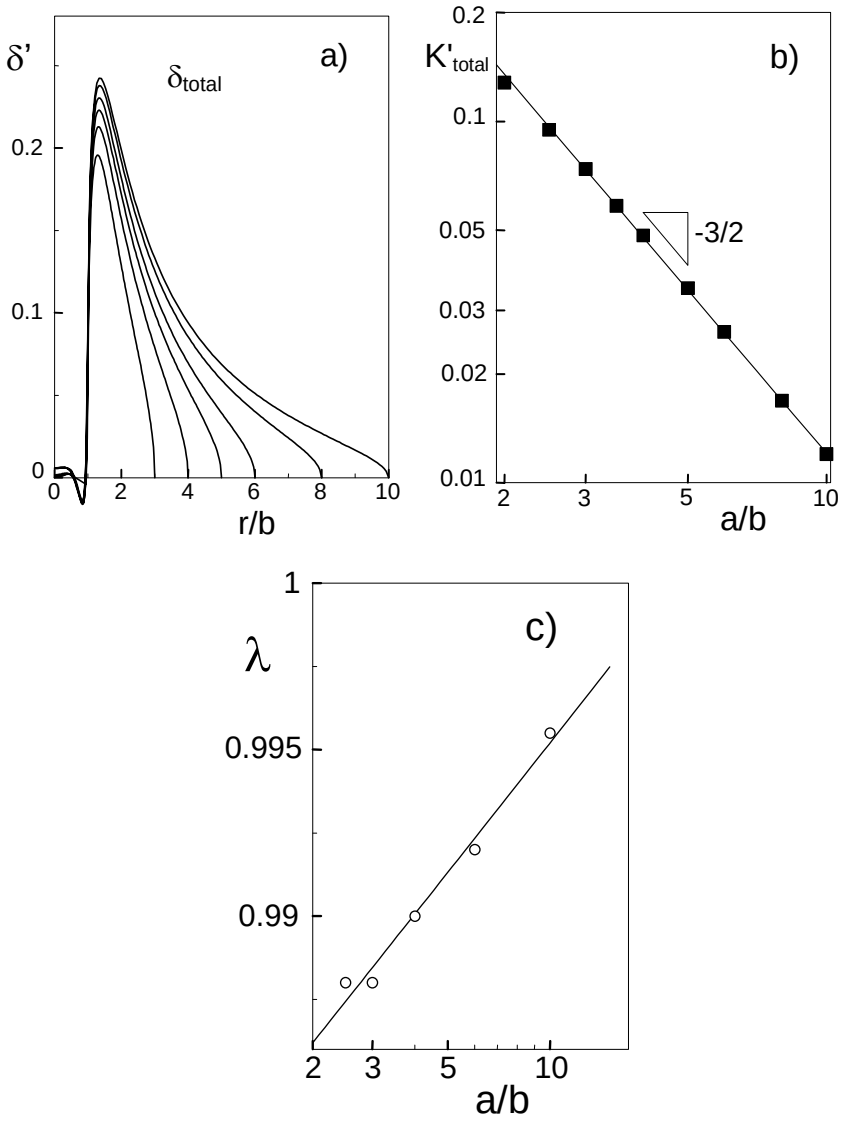

Fig. 9 a) Total crack opening displacement, b) normalised total stress intensity factor c) coefficient λ for eq.(25).

Based on the preceding considerations, an approximate analytical description of the total crack opening displacement can be given by [1]

$$\delta_{total} \cong -\frac{4ap}{\pi E'} g_1(a,b,r) + \frac{2bp}{\pi E'} g_2(a,b,r) + \frac{4ap^*}{\pi E'} g_1(a,\lambda b,r) \tag{25}$$

with

$$g_1(a,b,r) = \sqrt{1-(\tfrac{r}{a})^2}\,(1-\sqrt{1-(\tfrac{b}{a})^2}) + \\ + \tfrac{r}{a}[\mathbf{E}((\tfrac{b}{r})^2) - E(\arcsin\tfrac{r}{a},(\tfrac{b}{r})^2) - (1-(\tfrac{b}{r})^2)(\mathbf{K}((\tfrac{b}{r})^2) - F(\arcsin\tfrac{r}{a},(\tfrac{b}{r})^2))] \tag{26a}$$

$$g_2(a,b,r) = \tfrac{b}{r}[\mathbf{E}((\tfrac{b}{r})^2) - E(\arcsin(\tfrac{r}{a},(\tfrac{b}{r})^2)] \tag{26b}$$

$$p^*/p \cong 0.635 + 0.319b/a \tag{27}$$

$$\lambda \cong 0.9828\,(a/b)^{0.00565} \tag{28}$$

with λ represented in Fig. 9c. The unknown quantity p may be determined from the total stress intensity factor

$$K_{total} \cong \frac{2(p^*-p)}{\sqrt{\pi a}}\left(a-\sqrt{a^2-b^2}\right)+\frac{p}{\sqrt{\pi a}}\left(\frac{b}{a}\right)^2\sqrt{a^2-b^2} \tag{29}$$

in combination with Fig. 9b or eq.(23).

Expressed by the stress intensity factor, the displacements read

$$\delta = \frac{4K\sqrt{a}}{0.382\,\pi E'}\left(\frac{a}{b}\right)^2\left[\frac{b}{2a}\,g_2(a,b,r)+(0.635+0.319b/a)g_1(a,b,r)-g_1(a,\lambda b,r)\right] \tag{30}$$

This relation is suited for evaluating experimentally determined COD profiles as will be illustrated in section 4.

3. Superposition of external stresses

3.1. Applied stress intensity factor and displacement

Very often, Vickers indentation cracks are used for fracture mechanics tests under superimposed loading. Such additional loads may be caused by residual stresses or externally applied loads (tension, bending).

The crack opening displacement field under a constant externally applied stress $\sigma=\sigma_{appl}$, denoted by δ_{appl}, is given by the well-known elliptical profile

$$\delta_{appl} = \frac{4\sigma_{appl}}{\pi E'}\sqrt{a^2 - r^2} \tag{31}$$

i.e. by

$$\delta'_{appl} = \frac{\sigma'_{appl}}{p}\frac{a}{b}\sqrt{1-(r/a)^2} \tag{32}$$

The contact stresses under an external load can now be determined by solving

$$\begin{aligned} &\delta_{total} = \delta_{res} + \delta_{cont} + \delta_{appl} = 0 \quad for \quad r \le d \\ &\sigma_{cont} = 0 \qquad\qquad\qquad\qquad\quad for \quad r > d \end{aligned} \tag{33}$$

The computations mentioned in section 2 are now repeated for several stress ratios σ_0/p. Figure 10 shows the contact stresses at various externally applied stresses. It is obvious that the contact stresses decrease with increasing applied stress, as has to be expected from the fact that the boundary conditions are displacement-controlled and not stress-controlled.

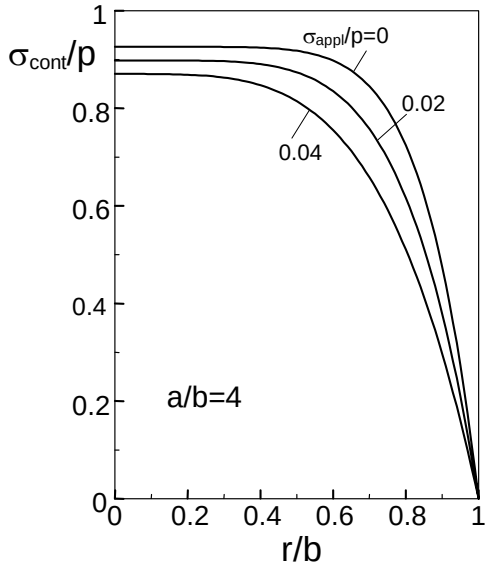

Fig. 10 Contact stresses at various externally applied stresses, computed under the assumption *d=b*.

Similar to eqs.(19a) and (19b), the contact stresses can be described by

$$\sigma_{cont} = D(1-(r/b)^q)\,p \tag{34}$$

with the parameters *D*, *q* shown in Fig. 11 as functions of the applied loading.

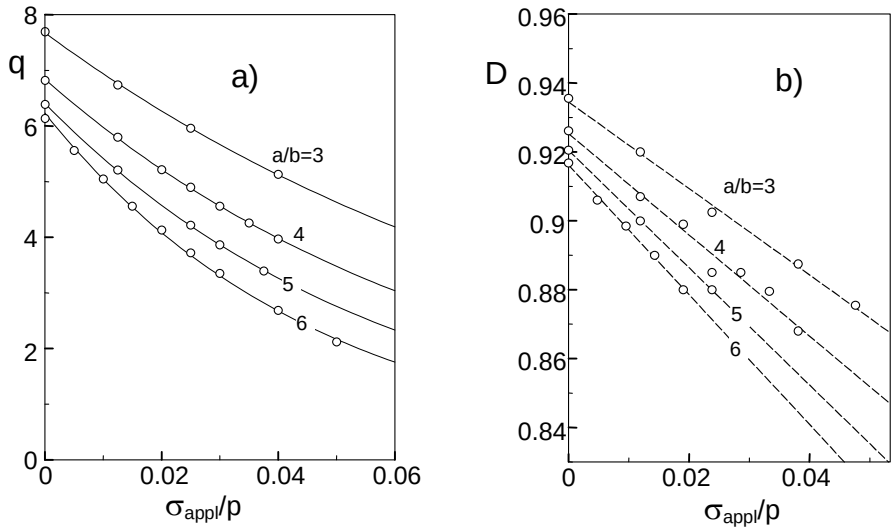

Fig. 11 Parameters *q* and *D* of the contact stresses according to eq.(34).

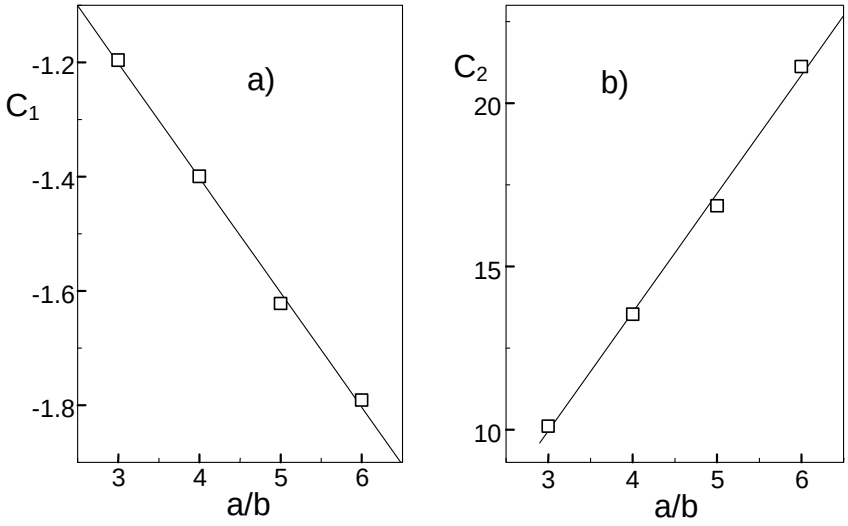

Fig. 12 Fit of numerically determined parameters.

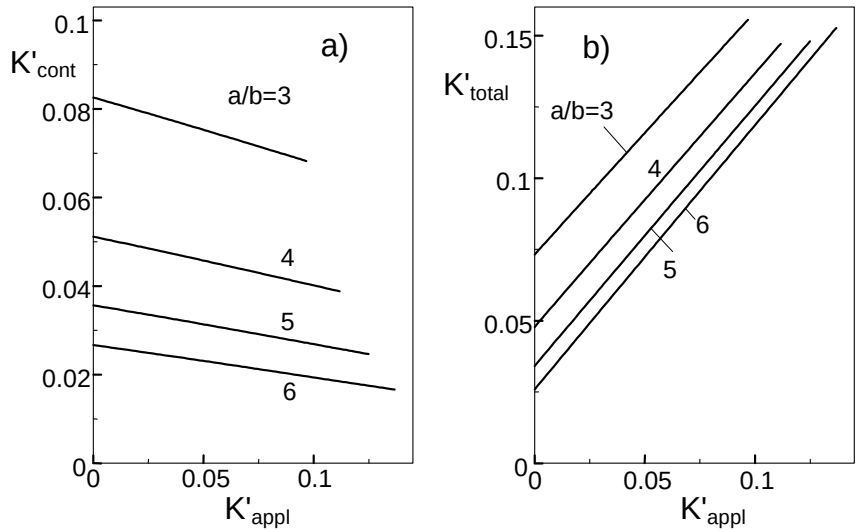

Fig. 13 Contact and total stress intensity factors as a function of the applied stress intensity factor at an externally applied stress of $0 \le \sigma_{appl}/p \le 0.05$.

For $\sigma_{appl}/p<0.05$ and $2.5<a/b<6$ an approximate representation of D and p reads

$$D \cong D_0 + C_1 \frac{\sigma_{appl}}{p} \tag{35}$$

$$C_1 = -0.6 - 0.2\frac{a}{b} \tag{36}$$

$$q \cong q_0 \exp\left[- C_2 \frac{\sigma_{appl}}{p} \right] \tag{37}$$

$$C_2 = 3.64\frac{a}{b} - 0.96 \tag{38}$$

with the coefficients C_1, C_2 plotted in Fig. 12 and D_0, q_0 given by eqs.(19b) and (19c).

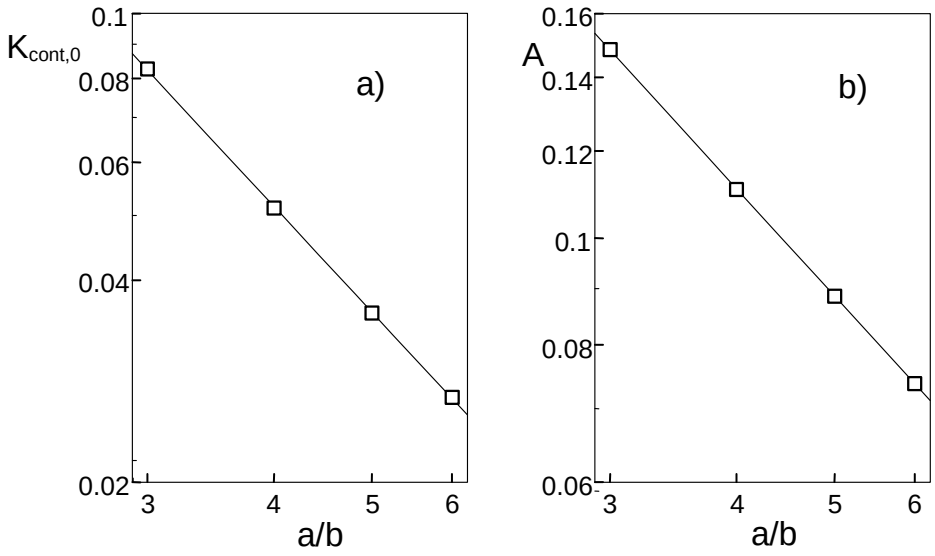

Fig. 14 Coefficients for eq.(39) as a function of a/b.

In Fig. 13 the contact and total stress intensity factors are plotted versus the applied stress intensity factor. The curves given in Fig. 13a may be approximated by straight lines

$$K'_{cont} = K'_{cont,0} + AK'_{appl} \tag{39}$$

with

$$K'_{appl} = \frac{2}{\sqrt{\pi}} \frac{\sigma_{appl}}{p} \sqrt{\frac{a}{b}} \tag{40}$$

and $K'_{cont,0}$, A represented in Fig. 14. A least-squares fit of these data for $3 \le a/b \le 6$ results in

$$K'_{cont,0} = 0.492\,(b/a)^{1.627} \tag{41}$$

and

$$A = -0.4487\,(b/a)^{1.008} \tag{42}$$

Consequently, the total stress intensity factor (Fig. 13b) may be expressed by

$$K'_{total} = K'_{total,0} + (A+1)K'_{appl} \tag{43}$$

with the total stress intensity factor $K'_{total,0}$ in the absence of an externally applied load being

$$K'_{total,0} = K'_{res} + K'_{cont,0} \tag{44}$$

$K'_{total,0}$ can be computed by use of the approximate power law relations (10) and (41). The result is plotted as the squares in Fig. 15. A power law fit of these data again yields the exponent –3/2 as given by eq.(23). It is self-evident that the difference of two stress intensity factor contributions depending on different powers in a/b can be represented by a common power dependency in a narrow band of a/b ratios only (here in $2.5<a/b<6$).

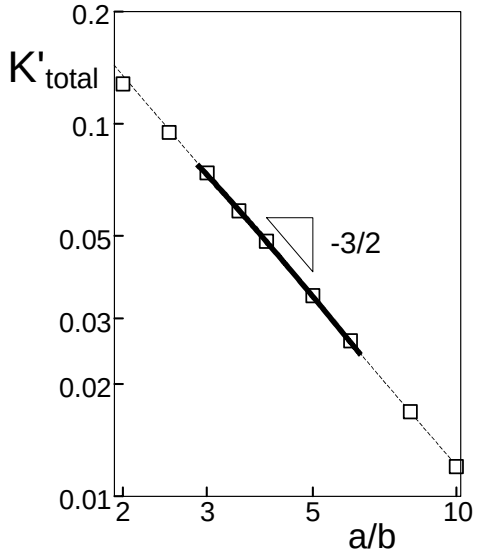

Fig. 15 Power representation of eq.(43) for $K'_{appl}=0$.

3.2 Impacts of variable contact stresses on crack extension under an externally applied load

As found out in section 3.1, the contact stress intensity factor K_{cont} depends on the applied load. In order to illustrate the general effect of a decreasing contact stress intensity factor with an increasing externally applied stress intensity factor on crack extension, the case of a material without an R-curve behaviour may be considered. A crack of initial size $a=3b$ is assumed to be present after a Vickers indentation test. The total stress intensity factor in this state is K_{Ic}.

In the normalised representation according to eq.(9) it reads

$$K'_{Ic} = \frac{K_{Ic}}{p\sqrt{b}} \tag{45}$$

In Fig. 16 the variation of the different stress intensity factors with crack size is illustrated for several values of the applied stress σ_{appl}. Figure 17a shows the total stress intensity factor for

several applied stresses that are necessary to propagate a crack of initial size a/b=3. The circle indicates the strength, i.e. the point at which

$$K'_{total} = K'_{Ic} \tag{46a}$$

$$\frac{\partial K'_{total}}{\partial (a/b)} = 0 \tag{46b}$$

are fulfilled. The related applied stress intensity factor is given in Fig. 17b.

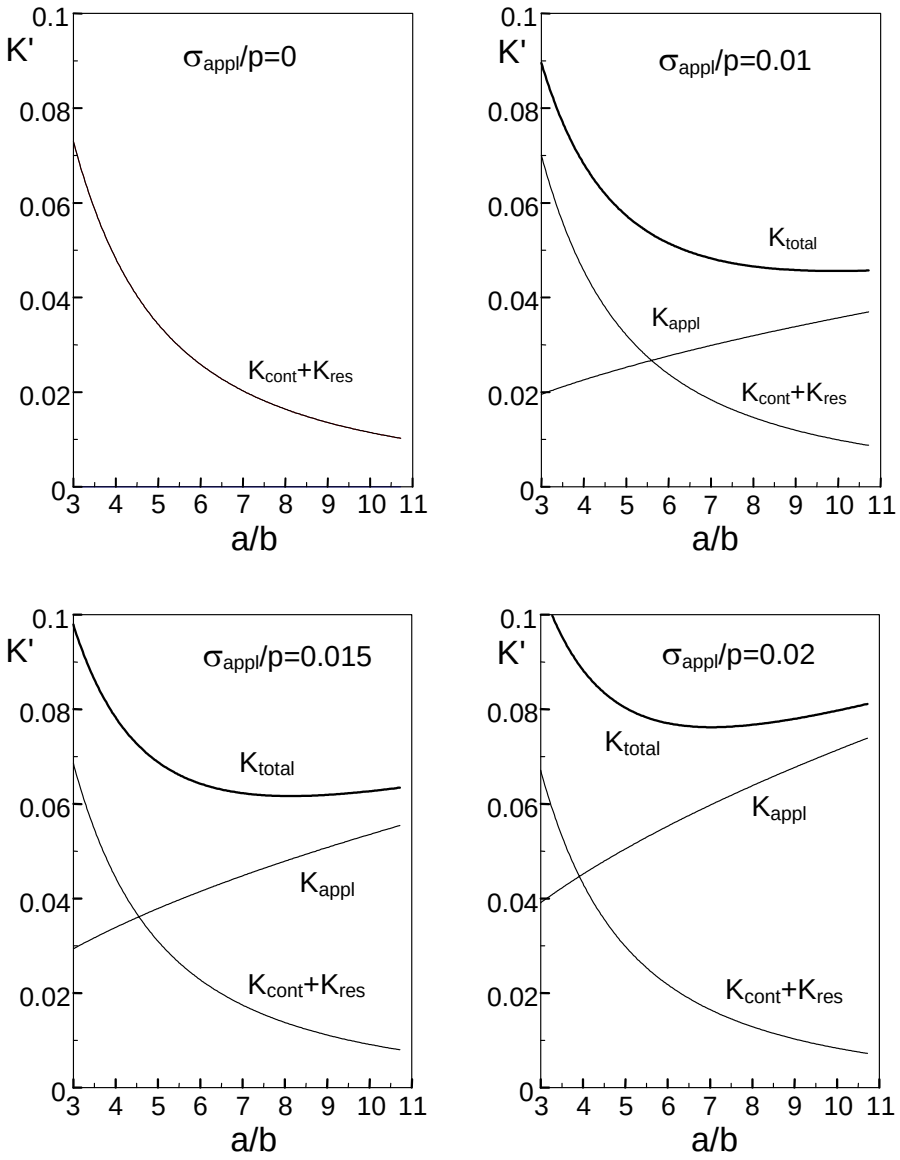

Fig. 16 Total stress intensity factor K_{total} and its components as a function of crack size.

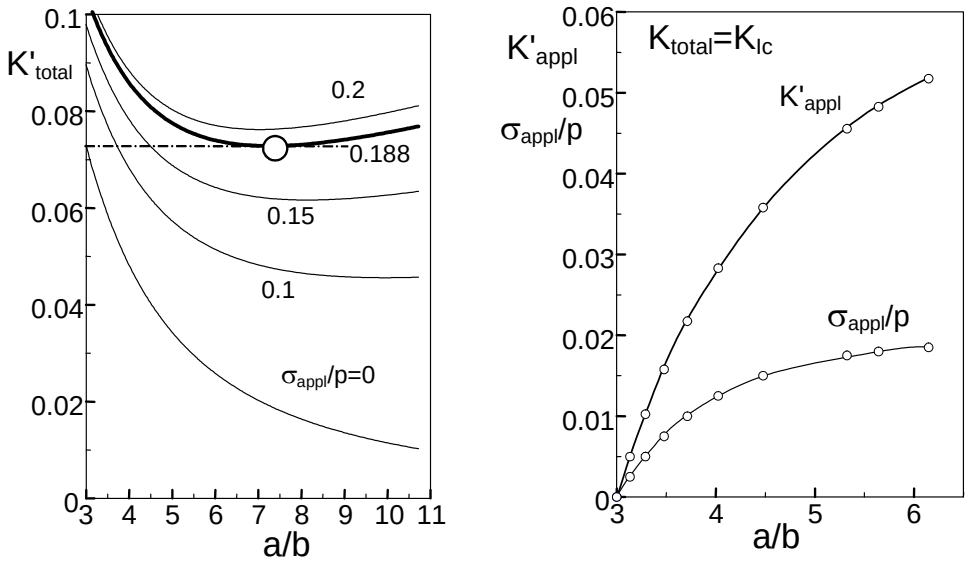

Fig. 17 a) Total stress intensity factor for several applied stresses, b) applied stress and stress intensity factor necessary to propagate a crack of initial size a/b=3.

4. Determination of *K* from the COD profile

As an example of application, the crack tip stress intensity factor K_{tip} may be determined for a (70% SiO_2, 19% CaO, and 15% Na_2O) soda-lime glass (E=71 GPa, ν=0.22) [5]. In Fig. 18 crack opening displacement measurements are plotted as circles. The results were measured at an indentation crack introduced under 50 N load by using a SEM. In order to avoid subcritical crack growth during the measuring time span, the specimen was suspended for 1 h in air after indentation.

In Fig. 18b the measured crack opening displacements δ_{meas} are plotted versus the displacements δ_{comp} computed from eqs.(25-30) for an arbitrarily chosen stress intensity factor of K = 1MPa√m. A least-squares fit of the linear dependency yields K as the slope of the straight line, in the present example resulting in K = 0.38 MPa√m. Use of this value then yields the solid curve introduced in Fig. 18a. The dashed line shown in Fig. 18a corresponds to the Irwin solution for the near-tip displacement field

$$\delta_{near\ tip} \rightarrow \sqrt{\frac{8}{\pi}} \frac{K}{E'} \sqrt{a-r} \tag{47}$$

at the same stress intensity factor of K = 0.38 MPa√m. This value is roughly identical with the threshold value K_{th} in air [6], below which no subcritical crack growth occurs.

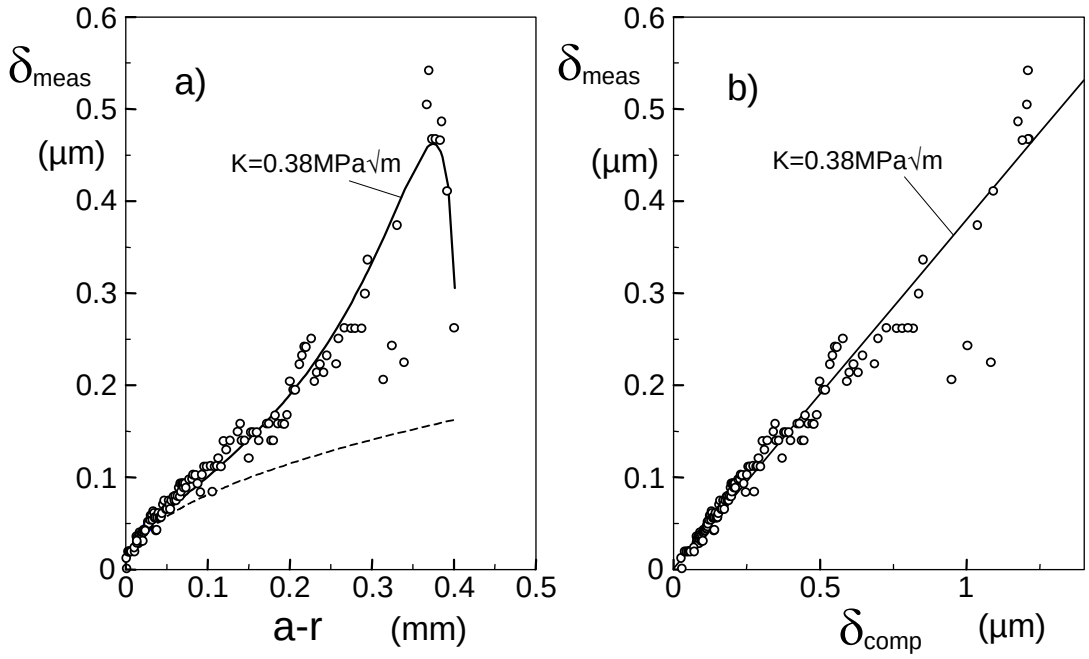

Fig. 18 Determination of K_{tip} for a soda-lime glass, a) measured crack opening displacement, b) measured COD plotted versus computed COD (K=1 MPa√m).

II FINITE ELEMENT STUDY

5. Stress intensity factor and T-stress

In the first part of this report the problem of a penny-shaped crack was treated with semi-analytical methods. This approach is of advantage for the derivation of analytical relations describing the principal shape of crack opening profiles. For special problems which cannot be solved with the weight functions available, we also applied the Finite Element (FE) method. For instance, the FE method was used to determine the T-stress under the complicated indentation crack loading. Moreover, the FE computations allow to check the accuracy of semi-analytical results.

5.1 Importance of T-stress

The fracture behaviour of cracked structures is dominated by the near-tip stress field. In fracture mechanics particular interest is devoted to stress intensity factors which describe the singular stress field ahead of a crack tip and govern fracture of a specimen when a critical stress intensity factor is reached. Nevertheless, there is experimental evidence of fracture mechanics properties being also affected by the constant stress contributions acting over a longer distance from the crack tip.

Taking into consideration the singular stress term and the first regular term, the near-tip stress field can be described by

$$\sigma_{ij} = \frac{K_I}{\sqrt{2\pi r}} f_{ij}(\varphi) + \sigma_{ij,0} \tag{48}$$

with the angular functions for mode I

$$f_{xx} = \cos\left(\frac{\varphi}{2}\right)\left[1 - \sin\left(\frac{\varphi}{2}\right)\sin\left(\frac{3\varphi}{2}\right)\right] \tag{49a}$$

$$f_{yy} = \cos\left(\frac{\varphi}{2}\right)\left[1 + \sin\left(\frac{\varphi}{2}\right)\sin\left(\frac{3\varphi}{2}\right)\right] \tag{49b}$$

$$f_{xy} = \cos\left(\frac{\varphi}{2}\right)\sin\left(\frac{\varphi}{2}\right)\cos\left(\frac{3\varphi}{2}\right) \tag{49c}$$

(r and φ are polar coordinates with the origin at the crack tip) and

$$\sigma_{ij,0} = \begin{pmatrix} \sigma_{xx,0} & \sigma_{xy,0} \\ \sigma_{yx,0} & \sigma_{yy,0} \end{pmatrix} = \begin{pmatrix} T & 0 \\ 0 & 0 \end{pmatrix} \tag{50}$$

The term T represents the total constant σ_x-stress contribution appearing at the crack tip ($x = a$) of a *cracked structure*, which is called the T-stress. It may be determined by evaluating the stresses ahead of a crack tip for y=0 and $x \to a$

$$T = (\sigma_x - \sigma_y)\big|_{x=a} \,. \tag{51}$$

The biaxiality ratio β proposed by Leevers and Radon [7]

$$\beta = \frac{T\sqrt{\pi a}}{K_I} \tag{52}$$

represents the T-stress in a normalised form. This ratio governs path stability of cracks growing under mixed-mode conditions as shown by Cotterell and Rice [8]. Their most important conclusion is illustrated in Fig. 19, namely, increasing deviation from the prescribed kink angle Θ_0 for $T>0$ ($\beta>0$) and decreasing deviations for $T<0$ ($\beta<0$).

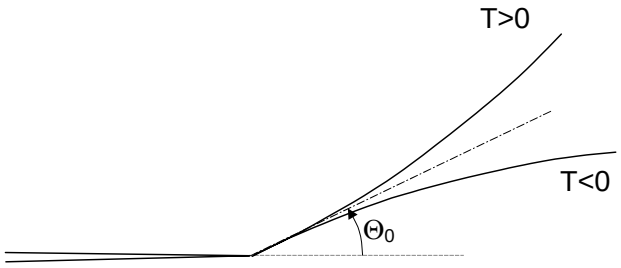

Fig. 19 General influence of the T-stress after crack kinking under mixed-mode loading.

5.2 Penny-shaped crack in an infinite body under remote tension

In order to check the Finite Element (FE) net, the penny-shaped crack in an infinite body under remote tension was studied. In this case (Fig. 20) the stress intensity factor solution is analytically known as

$$K = F\sigma\sqrt{a}\,, \quad F = \frac{2}{\sqrt{\pi}} \tag{53}$$

The case of an infinite body with a penny-shaped internal crack was realized by a finite element net of about 2000 elements with 6300 nodes and a component height of H=100a and component width of W=100a under rotational symmetry conditions. The computations were carried out with ABAQUS Version 6.2 which provides the stress intensity factors K_I as well as the T-stress term. The numerically obtained stress intensity factor was

$$F_{FE} = 1.1285 \tag{54}$$

deviating about 0.01% from the exact solution. The T-stress computed for several Poisson's ratios ν was found to be

$$T/\sigma = -0.51 - \nu \tag{55a}$$

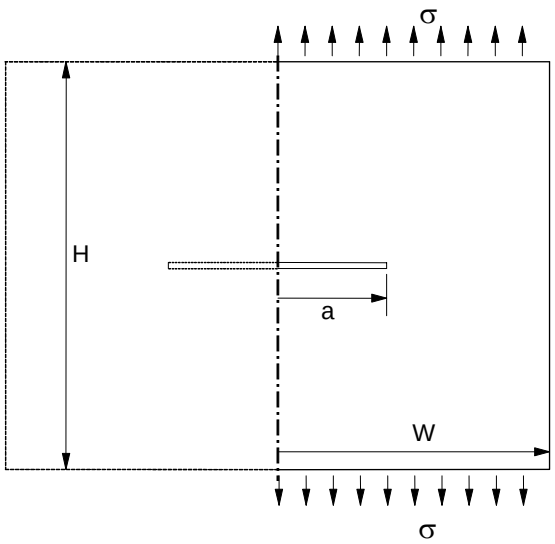

Fig. 20 Circular crack in an infinite body.

5.3 Penny-shaped crack under crack-face loading

A loading situation resulting in the same stress intensity factor solution as under constant remote tension is given by a constant normal crack face pressure p. The x-stresses were found to be identical with those for remote tension and the T-stress term, T_{cf} (subscript "cf" standing for "crack face" loading), was

$$T_{cf} / | p | = T / \sigma + 1 = 0.49 - \nu \tag{55b}$$

The difference between eqs.(55a) and (55b) is caused by the different values of $\sigma_y|_{r=a}$ in the two loading cases. Whereas $\sigma_y|_{r=a}=0$ under remote tension (crack faces are free of normal stresses), $\sigma_y|_{r=a}= -p_0$ under crack-face pressure conditions. Consequently, the T-stress resulting from eq.(61) for the same amount of σ_x stress is different by $-p_0$.

In a second example, the normal stresses were prescribed on the crack faces similar to the residual stress distribution eq.(4a). The crack opening displacement behaviour under loading by these residual stresses was modelled by crack face pressure for $r>b$ that causes positive displacements and tensile stresses on the crack faces in the region of $0 \le r \le b$, which will close the crack (Fig. 21), i.e.

$$\sigma_{cf} = \sigma_0 \quad \text{for} \quad r \le b \quad , \quad \sigma_{cf} = -\tfrac{1}{2}\sigma_0 (r/b)^3 \quad \text{for} \quad r > b \tag{56}$$

In order to prevent crack penetration, the element-based contact surface option of ABAQUS 6.2 was chosen. The number of elements and nodes of the FE net was increased by about 50%. The additional nodes were introduced near the location $r=b$ to obtain the size of the contact zone as accurately as possible. For the further computations it was chosen $W=H=100b$.

In Fig. 22 the results for the special case of $a/b=4$ are presented. In Fig. 22a the displacements are plotted as the circles. From these results, the size of the contact zone d is obtained as $d=0.95b$. The curve in this figure represents the semi-analytical result. The agreement is good. An increased accuracy is reached for $r/b>2$ by setting $\lambda=1$ in eq.(25) or (30). This can be seen from Fig. 22b. Equation (30) is then simplified to

$$\delta = \frac{4K\sqrt{a}}{0.382\,\pi E'}\left(\frac{a}{b}\right)^2\left[\frac{b}{2a}\,g_2(a,b,r) - (0.365 - 0.319b/a)g_1(a,b,r)\right] \qquad (57)$$

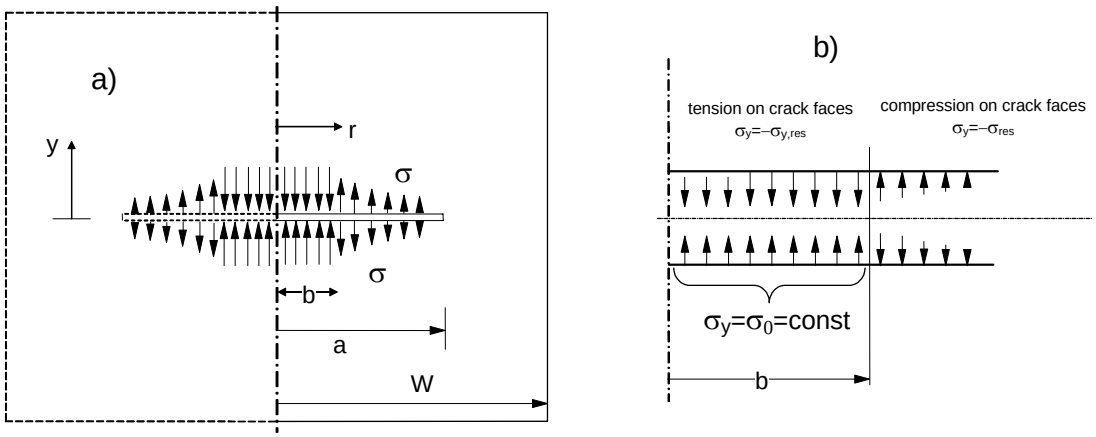

Fig. 21 Circular crack in an infinite body a) loaded by the normal component of residual stresses, b) realisation in FE computation: crack closure by tensile tractions in $r<b$, crack face pressure for $r>b$.

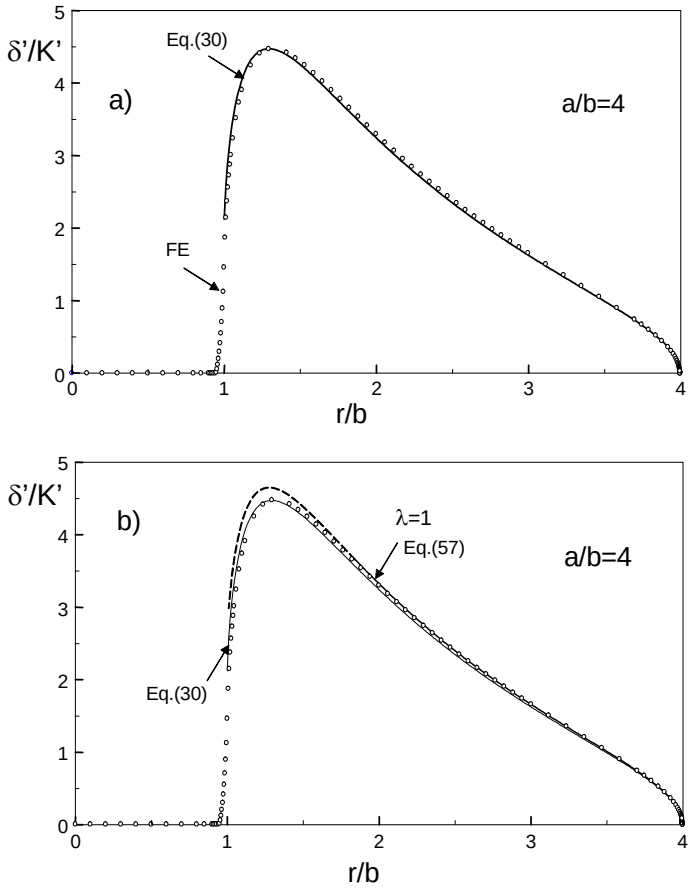

Fig. 22 a) COD profile computed by FE (circles) and by applying eq.(30) (curve), b) curve of improved accuracy for the region of $r/b>2$ represented by eq.(57).

The stresses σ_y for $y=0$ occurring under conditions of prevented crack face penetration are shown in Fig. 23a for a crack with $a/b=4$. As expected, they are in agreement with the crack

face loading outside $r=d$ (note that the crack face loading has a different sign compared with the residual stresses in the uncracked body). Figure 23b shows the influence of the crack size a on the size b of the contact zone. The result may be expressed as

$$d / b \cong 0.9655(a / b)^{-0.0135} \tag{58}$$

In the contact region $r \le d$, the difference of the prescribed surface tractions and the stresses σ_y for $y=0$ provides the contact stresses σ_{cont} as defined in Section 2.4. The result is given in Fig. 27 by the circles, whereas the curve represents the result of Fig. 10 for $\sigma_{appl}/p=0$. The difference between the results is due to the simplifying assumption of $d=b$ used in the semi-analytical analysis. In principle, the solid curve in Fig. 24 is an effective continuous fitting curve over $0<r<b$ for the FE data distributed over $0<r<0.95b$, resulting in the same normalised crack opening displacement profile δ'/K' at $r>b$.

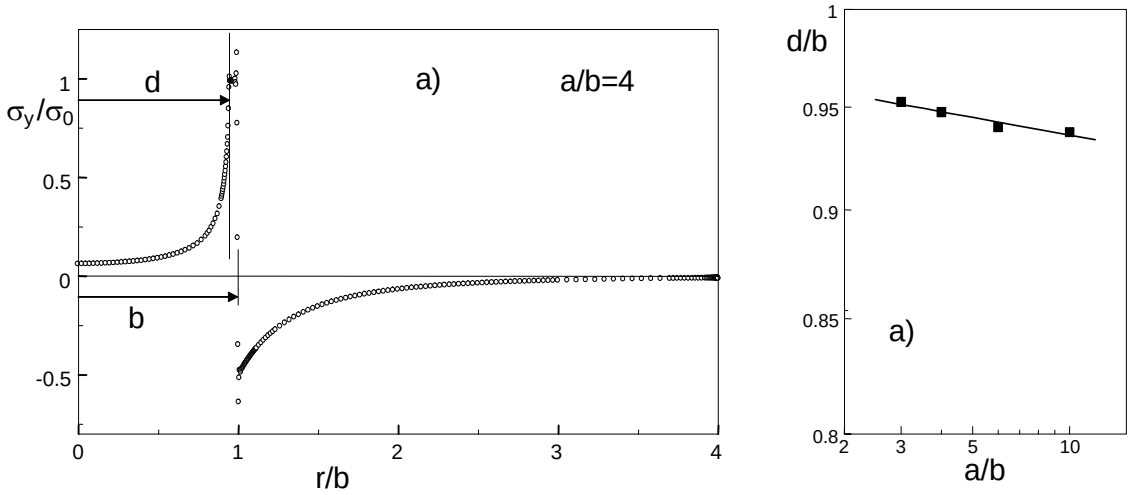

Fig. 23 a) Normal stresses σ_y at $y=0$, b) contact zone radius d as a function of the ratio a/b.

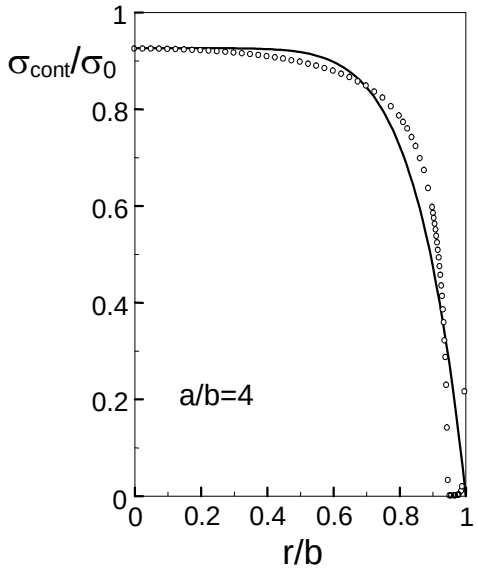

Fig. 24 Contact stresses according to eq.(15) resulting from the difference of the stresses in Fig. 23a and the presribed crack face tractions.

In Fig. 25a the stress intensity factor in the normalisation of eq.(9) is plotted versus the crack size. The result can be expressed by

$$K' = \frac{0.382}{(a/b)^{3/2}} \tag{59}$$

which is in very good agreement with eq.(23).

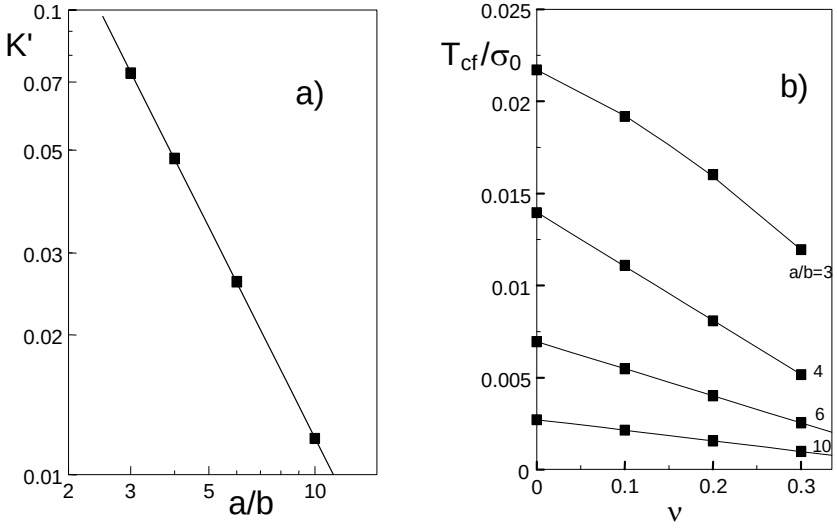

Fig. 25 a) Stress intensity factor as function of the crack size, b) influence of Poisson's ratio on T-stress under crack face loading.

The T-stress solution for the special crack face loading (Fig. 21b) is shown in Fig. 25b as a function of Poisson's ratio. For $a/b \geq 4$ a linear influence of ν is found. From the T-stress representation in Fig. 26a, a crack size dependency given by a power law in a/b can be concluded. Therefore, the T-stress term under crack face loading is approximated for $a/b > 3.5$ as

$$T_{cf} / \sigma_0 \cong \frac{0.1702 - 0.3581\nu}{(a/b)^{9/5}} \tag{60}$$

The T-stress under a residual stress exhibiting a normal stress component $\sigma_{y,res} = -\sigma_{cf}$ only is then given as

$$T = T_{cf} + \sigma_{cf}\Big|_{r=a} \tag{61}$$

and in the case of a σ_x-stress component already present in the uncracked body, $\sigma_{x,uncracked}$, it finally holds

$$T = T_{cf} + \sigma_{cf}\Big|_{r=a} + \sigma_{x,uncracked}\Big|_{r=a} \tag{62}$$

From the model of a cavitation under an internal pressure p, the radial stress component is obtained as

$$\sigma_{x,uncracked}\Big|_{r=a} = \sigma_{r,res}\Big|_{r=a} = -p(b/a)^3 \tag{63}$$

and the T-stress for the residual stress problem reads

$$T / p \cong \frac{0.1702 - 0.3581\nu}{(a/b)^{9/5}} - \tfrac{3}{2}(b/a)^3 \tag{64}$$

This dependency is illustrated in Fig. 26b for Poisson's ratios of ν=0.2 and 0.3 as representative values of ceramics.

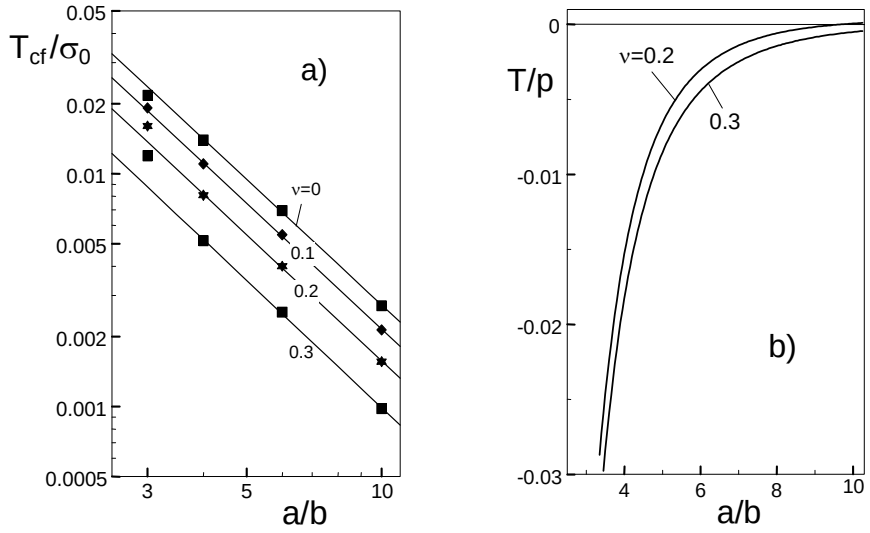

Fig. 26 a) Influence of Poisson's ratio and crack size on the T-stress under crack face loading, b) T-stress for the residual stress problem.

5.4 Penny-shaped crack under superimposed internal stresses and remote tension

The computations made in Section 5.2 were repeated under the condition of a superimposed external stress σ_{appl}. Whereas in the semi-analytical analysis a constant contact area was assumed (e.g. Section 3.1), the finite element solution automatically provides a more realistic solution under a variable and also disappearing contact region. Figure 27a shows the crack profiles for a crack with a/b=4 under this combined loading. It becomes obvious that the region where the surfaces are in contact decreases with increasing applied stress. In Fig. 27b the radius of the contact area is plotted as a function of a/b and σ_{appl}/σ_0. Figure 28 finally represents the effective stress intensity factor K'_{total} as a function of the externally applied stress intensity factor K'_{appl}. All data are beyond the dashed line which illustrates the condition $K_{total}=K_{appl}$ asymptotically valid for large cracks.

The data of Fig. 28 were fitted in the region in which crack surface contact did not disappear totally, the results being

$$K'_{total} = \frac{0.382}{(a/b)^{3/2}} + [1 - 0.52(a/b)^{5/4}]K'_{appl} \tag{65}$$

$$T / \sigma_0 \cong \frac{0.0986}{(a/b)^{9/5}} - 0.77\frac{\sigma_{appl}}{\sigma_0} \quad \text{for} \quad \nu=0.2 \tag{66}$$

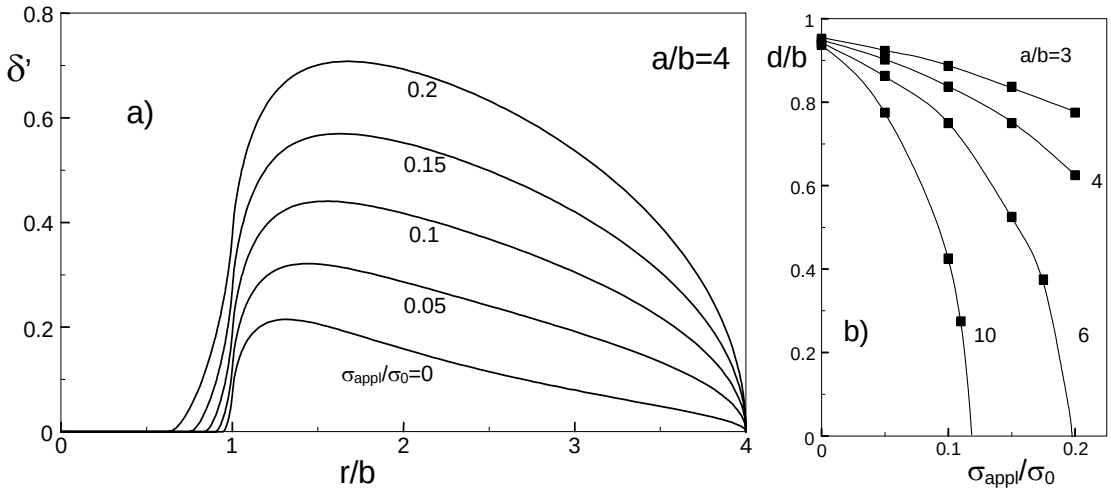

Fig. 27 a) Crack opening profiles under superimposed remote tensile load, b) size of the contact zone.

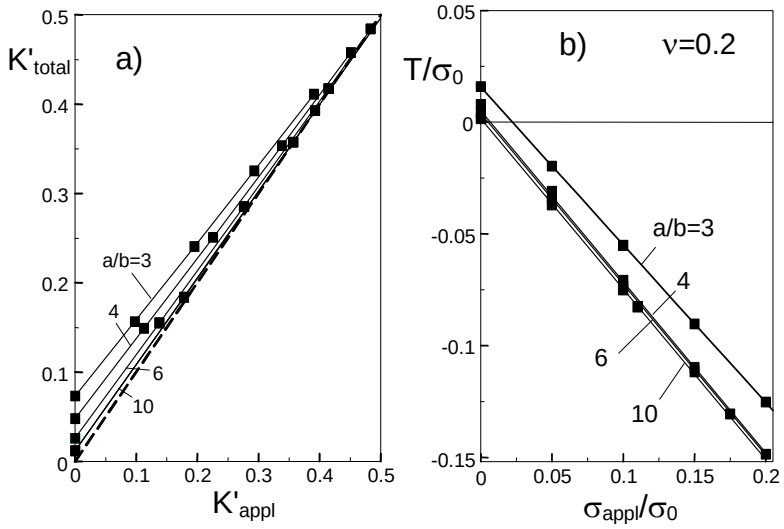

Fig. 28 a) Total stress intensity factor K'_{total} as a function of the externally applied stress intensity factor K'_{appl} for several crack lengths, b) T-stress solution.

III SUMMARY OF RESULTS FOR VICKERS CRACKS

The semi-analytical study in combination with the FE analysis leads to the following results that are again summarised below.

Loading by a residual stress field
Computation is based on the residual stress field with stresses normal to the crack face

$$\sigma_{res} = \begin{cases} -p_0 & \text{for } r < b \\ \frac{1}{2} p_0 (b/r)^3 & \text{for } r > b \end{cases} \tag{III.1}$$

For a sufficient representation of the total COD including the maximum near $r/b \approx 1.3$, it may be used

$$\delta = \frac{4K\sqrt{a}}{0.382\,\pi E'} \left(\frac{a}{b}\right)^2 \left[\frac{b}{2a} g_2(a,b,r) + (0.635 + 0.319 b/a) g_1(a,b,r) - g_1(a,\lambda b,r) \right] \tag{III.2}$$

with

$$\begin{aligned} & g_1(a,b,r) = \sqrt{1-(\tfrac{r}{a})^2}\,(1-\sqrt{1-(\tfrac{b}{a})^2}) + \\ & + \tfrac{r}{a}[\mathbf{E}((\tfrac{b}{r})^2) - E(\arcsin\tfrac{r}{a},(\tfrac{b}{r})^2) - (1-(\tfrac{b}{r})^2)(\mathbf{K}((\tfrac{b}{r})^2) - F(\arcsin\tfrac{r}{a},(\tfrac{b}{r})^2))] \end{aligned} \tag{III.3}$$

$$g_2(a,b,r) = \tfrac{b}{r}[\mathbf{E}((\tfrac{b}{r})^2) - E(\arcsin(\tfrac{r}{a},(\tfrac{b}{r})^2)] \tag{III.4}$$

$$\lambda \cong 0.9828\,(a/b)^{0.00565} \tag{III.5}$$

The crack-opening displacements for $r>1.5b$ can be described by $\lambda=1$, i.e.

$$\delta = \frac{4K\sqrt{a}}{0.382\,\pi E'} \left(\frac{a}{b}\right)^2 \left[\frac{b}{2a} g_2(a,b,r) - (0.365 - 0.319 b/a) g_1(a,b,r) \right] \tag{III.6}$$

The size of the contact zone, d, is approximately given by

$$d/b \cong 0.9655 (a/b)^{-0.0135} \tag{III.7}$$

The total stress intensity factor (superimposed by residual and contact stress intensity factor contributions) holds

$$K = \sigma_0 \sqrt{b}\, \frac{0.382}{(a/b)^{3/2}} \tag{III.8}$$

The related T-stress term for $a/b>3.5$ results as

$$T / p \cong \frac{0.1702 - 0.3581\nu}{(a/b)^{9/5}} - \tfrac{3}{2}(b/a)^3 \qquad \text{(III.9)}$$

Loading by superimposed externally applied stresses

In the presence of an externally applied remote stress σ_{appl}, the total stress intensity factor is

$$K'_{total} = \frac{0.382}{(a/b)^{3/2}} + [1 - 0.52(a/b)^{5/4}]K'_{appl} \qquad \text{(III.10)}$$

and the T-stress under crack face loading at ν=0.2 equals according to eq.(56)

$$T / \sigma_0 \cong \frac{0.0986}{(a/b)^{9/5}} - 0.77\frac{\sigma_{appl}}{\sigma_0} \qquad \text{(III.11)}$$

CONE CRACKS

6 Cone crack formation

Under spherical contact loading, cone cracks are initiated in brittle materials (see Fig. 29). The crack opening angle φ was found to be in the range of 21°≤φ≤31°, depending on the material tested. An extended overview is given in a paper of Kocer and Collins [9]. Several studies were performed on soda-lime glass with the result of φ~21.5±1° [6, 9-11]. Several attempts have been made so far to compute these cone angles [12-15]. Very early, the crack angle was determined by Frank and Lawn [12] using a simplified weight function procedure (see also [14] and [15]). In these papers, the general crack shape is assumed to coincide with the stress trajectories in the uncracked body and the cone angle concluded from the condition of maximum energy release rate. Frank and Lawn [12] determined the stress intensity factor K_I for a crack extending along the trajectory of the minimum principal stress

$$K_I = \int_0^c \sigma_n h \, dr \tag{67}$$

with the normal stress σ_n along the crack present in the uncracked body and the (asymptotic) weight function

$$h = \frac{2\sqrt{c}}{\sqrt{\pi(c^2 - r^2)}} \tag{68}$$

The crack angle was obtained from the condition of maximum energy release rate given as

$$G = \frac{1-\nu^2}{E} K_I^2 \tag{69}$$

A numerical analysis was given by Kocer and Collins [9], where step-wise crack extension calculations were performed for loading by a flat punch using finite elements. In these considerations also the maximum energy release rate criterion was applied for describing the local crack direction.

The agreement of the two methods is quite poor. Whereas the weight function computations need an unrealistically high Poisson's ratio of ν=0.33 for the experimentally found cone crack angle of ~22° of soda-lime glass, the FE study of [9] showed an excellent agreement with the experiments for the realistic value of ν=0.21. Therefore, the question arises where the discrepancies between the two procedures may come from. In this context it has to be noted that the weight function used in [12, 14, 15] is a very rough approximation only. Higher-order and mixed terms are completely missing.

It is the aim of our study to provide an improved weight function, including higher-order terms as well as mixed weight function contributions, and to disclose the errors made by application of the rough weight function approximation (68).

7 Weight functions

7.1 Weight function procedure

Figure 29a shows a sphere in contact with a plane surface. Under increasing load, a cone crack develops. In Fig. 29b this crack is shown in more detail. The relatively complicated parts near the free surface are ignored in the following considerations and replaced by a pure cone. The geometric data are given in Fig. 29c.

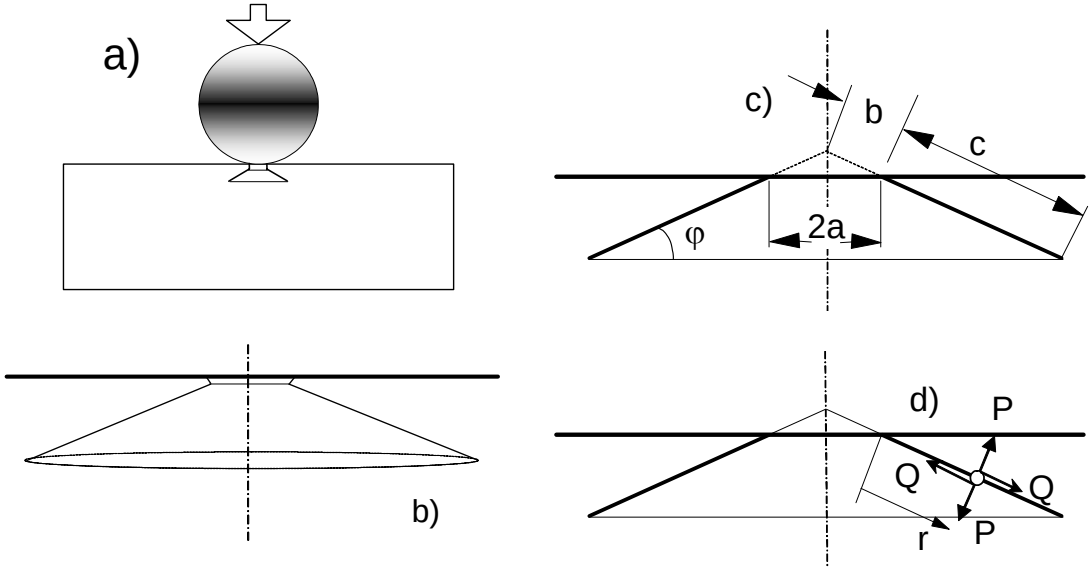

Fig. 29 a) Crack generation by a spherical indenter, b) cone crack, c) simplified geometry, d) couples of normal and shear forces for the determination of the weight functions.

The stress intensity factors K of cracks can be computed by the weight function method as

$$K_I = \int_0^c \sigma_n h_{11}(r,c)\, dr + \int_0^c \tau h_{12}(r,c)\, dr \tag{70a}$$

$$K_{II} = \int_0^c \sigma_\beta h_{21}(r,c)\, dr + \int_0^c \tau_{r\beta} h_{22}(r,c)\, dr \tag{70b}$$

where σ_n is the stresses in the uncracked body normal to the prospective crack plane and τ the shear stresses in this plane. The weight functions $h(r,c)$ are defined by [16]

$$h_{ij} = \sqrt{\frac{2}{\pi c}} \sum_{n=0}^{\infty} D_n^{(ij)} (1 - r/c)^{n-1/2} \tag{71a}$$

with $$D_0^{(11)} = D_0^{(22)} = 1\,, \quad D_0^{(12)} = D_0^{(21)} = 0 \tag{71b}$$

and including the asymptotic solution of

$$h = \sqrt{\frac{2}{\pi\,(c-r)}} \tag{72}$$

The contributions h_{ij} with i≠j are responsible for a mode-I stress intensity factor caused by the shear stress and a mode-II stress intensity factor caused by the normal stresses. Only in cases of high symmetry (e.g. an edge-cracked plate with the crack located exactly at half height) do the mixed terms disappear. The stresses of the Hertzian contact needed in eqs.(70a) and (70b) can be taken from the analysis of Huber [17]. To the authors knowledge, a weight function for cone cracks is not available. Therefore, this function has to be determined.

7.2 Weight function from FE computations

In order to determine the weight function, finite element computations were performed. The case of a semi-infinite body with a cone crack was realised by a finite element net of about 700 elements with 2500 nodes. The computations were carried out with ABAQUS, version 6.2 which provides the two stress intensity factors K_I and K_{II} from the displacement field.

The finite element computations were performed for couples of point forces *P* and *Q* on the crack at variable relative distance *r*/*c* from the crack tip (Fig. 29d). Since the weight function is the Green's function for stress intensity factors, the FE results for point forces directly provide the weight functions.

Figure 30 shows the weight functions obtained from the two point loads *P* (Fig. 30a) and *Q* (Fig. 30b) as the circles. It is of importance that mixed-mode stress intensity factor terms occur even under pure normal or shear force. Under load normal to the crack plane (*P*), also a mode-II stress intensity factor contribution and, consequently, a weight function h_{21} result, as obvious from Fig. 30a. Under pure shear load (*Q*), a mode-I stress intensity factor contribution is obtained which results in h_{12} (Fig. 30b). In the case of the weight functions h_{22} and h_{21}, no strong influence of φ and *b*/*c* was found. Taking into account the cone shape of the crack having an increasing circumference with increasing *r*, the set-up of eq.(71a) was modified into

$$h_{ij} = \sqrt{\frac{2}{\pi c}}\,\frac{r+b}{c+b}\sum_{n=0}^{\infty} D_n^{(ij)}(1-r/c)^{n-1/2} \tag{73}$$

From the FE results, the coefficients $D_n^{(ij)}$ were determined for ν=0.2 and 0.3 by application of a fit procedure. They are compiled in Tables 1 to 8.

There is a small influence of Poisson's ratio ν on the weight function components. This influence can be neglected in the case of weight functions h_{11} and h_{21}. A stronger influence was found for the contributions h_{11} and h_{12}, as obvious from Fig. 31 where the weight functions are plotted as functions of ν.

In order to obtain the full weight function solution in the range of 15≤φ≤30°, the data of Tables 1 to 8 may be interpolated with respect to *b*/*c*, ν, and φ. For a more simplified practical use, the coefficients are fitted as

$$D_n^{(ij)} = A_0 + A_1\varphi + A_2\varphi^2 + (A_3 + A_4\varphi + A_5\varphi^2)\frac{b}{c} \tag{74}$$

with the cofficients A_0-A_5 compiled in the Appendix in Table 9 for ν=0.2 and Table 10 for ν=0.3. For other ν values the weight function coefficients *D* may be computed from

$$D_n^{(ij)} = 10[D_n^{(ij)}(\nu = 0.3) - D_n^{(ij)}(\nu = 0.2)](\nu - 0.2) + D_n^{(ij)}(\nu = 0.2) \qquad (75)$$

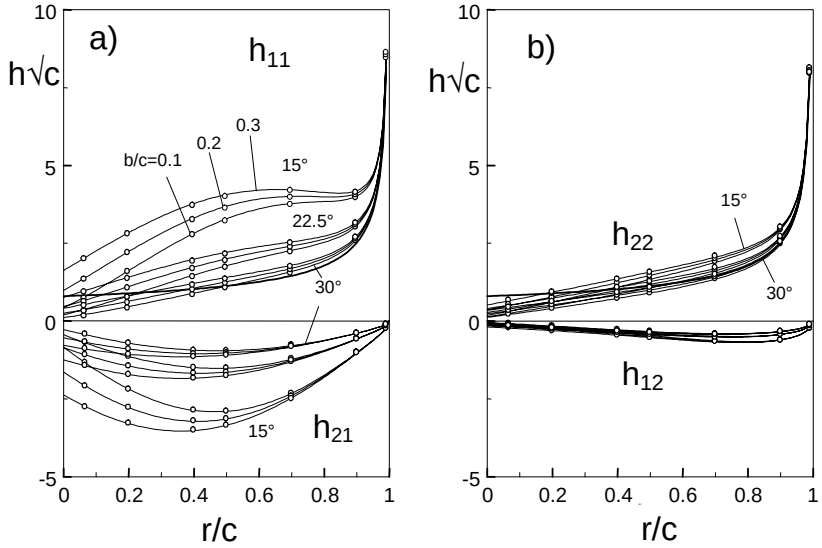

Fig. 30 Weight function from FE computations for b/c=0.1, 0.2, and 0.3 and several cone angles (thick curves: asymptotic solution, eq.(72)). a) Results obtained under normal force P, b) under shear force Q.

φ	b/c	$D_1^{(11)}$	$D_2^{(11)}$	$D_3^{(11)}$
15°	0.1	6.619	9.990	-11.762
	0.2	6.876	9.811	-10.282
	0.3	7.115	9.642	-8.936
22.5°	0.1	3.035	4.196	-5.438
	0.2	3.215	4.175	-4.902
	0.3	3.385	4.138	-4.371
30°	0.1	1.322	2.024	-2.798
	0.2	1.461	2.073	-2.640
	0.3	1.595	2.098	-2.445

Table 1 Coefficients of the weight function h_{11} (ν=0.2).

φ	b/c	$D_1^{(12)}$	$D_2^{(12)}$	$D_3^{(12)}$
15°	0.1	2.8468	-.6314	-.7125
	0.2	2.9530	-.7080	-.5530
	0.3	3.0349	-.7481	-.4694
22.5°	0.1	1.4316	.6574	-1.1476
	0.2	1.5367	.5997	-1.0457
	0.3	1.6204	.5662	-.9887
30°	0.1	.7130	.9232	-.9420
	0.2	.8127	.9024	-.9204
	0.3	.8948	.8889	-.9092

Table 2 Coefficients of the weight function h_{22} (ν=0.2).

φ	b/c	$D_1^{(21)}$	$D_2^{(21)}$	$D_3^{(21)}$
15°	0.1	-2.684	-18.200	9.410
	0.2	-2.750	-17.680	8.144
	0.3	-2.798	-17.332	7.280
22.5°	0.1	-1.654	-8.686	4.318
	0.2	-1.673	-8.495	3.729
	0.3	-1.690	-8.352	3.293
30°	0.1	-1.239	-4.841	2.299
	0.2	-1.235	-4.743	1.953
	0.3	-1.235	-4.664	1.680

Table 3 Coefficients of the weight function h_{21} (ν=0.2).

φ	b/c	$D_1^{(12)}$	$D_2^{(12)}$	$D_3^{(12)}$
15°	0.1	-2.990	3.952	-2.002
	0.2	-2.973	3.847	-1.891
	0.3	-2.961	3.770	-1.834
22.5°	0.1	-2.052	1.888	-.613
	0.2	-2.042	1.893	-.628
	0.3	-2.034	1.894	-.647
30°	0.1	-1.583	1.002	-.043
	0.2	-1.563	1.017	-.083
	0.3	-1.548	1.026	-.117

Table 4 Coefficients of the weight function h_{12} (ν=0.2).

φ	b/c	$D_1^{(11)}$	$D_2^{(11)}$	$D_3^{(11)}$
15°	0.1	6.558	10.589	-12.776
	0.2	6.843	10.301	-10.971
	0.3	7.107	10.041	-9.354
22.5°	0.1	2.971	4.463	-5.962
	0.2	3.170	4.403	-5.294
	0.3	3.359	4.327	-4.640
30°	0.1	1.235	2.188	-3.127
	0.2	1.391	2.217	-2.905
	0.3	1.540	2.221	-2.646

Table 5 Coefficients of the weight function h_{11} (ν=0.3).

φ	b/c	$D_1^{(12)}$	$D_2^{(12)}$	$D_3^{(12)}$
15°	0.1	2.9871	-.3460	-.9470
	0.2	3.0857	-.4384	-.7727
	0.3	3.1606	-.4964	-.6749
22.5°	0.1	1.5717	.8672	-1.3347
	0.2	1.6692	.7978	-1.2197
	0.3	1.7460	.7505	-1.1503
30°	0.1	.8587	1.0914	-1.1098
	0.2	.9503	1.0601	-1.0735
	0.3	1.0250	1.0358	-1.0503

Table 6 Coefficients of the weight function h_{22} (ν=0.3).

φ	b/c	$D_1^{(21)}$	$D_2^{(21)}$	$D_3^{(21)}$
15°	0.1	-2.7593	-18.5636	8.8931
	0.2	-2.8254	-17.9514	7.5379
	0.3	-2.8698	-17.5575	6.6635
22.5°	0.1	-1.7606	-8.9094	4.1169
	0.2	-1.7746	-8.6650	3.4623
	0.3	-1.7851	-8.4935	3.0023
30°	0.1	-1.3693	-4.9709	2.2173
	0.2	-1.3567	-4.8435	1.8217
	0.3	-1.3480	-4.7482	1.5254

Table 7 Coefficients of the weight function h_{21} (ν=0.3).

φ	b/c	$D_1^{(21)}$	$D_2^{(21)}$	$D_3^{(21)}$
15°	0.1	-2.9743	3.9767	-1.7737
	0.2	-2.9563	3.8605	-1.6732
	0.3	-2.9443	3.7756	-1.6281
22.5°	0.1	-2.0142	1.9440	-.4819
	0.2	-2.0052	1.9404	-.4994
	0.3	-1.9990	1.9338	-.5242
30°	0.1	-1.5091	1.0672	.0271
	0.2	-1.4941	1.0764	-.0100
	0.3	-1.4835	1.0796	-.0447

Table 8 Coefficients of the weight function h_{12} (ν=0.3).

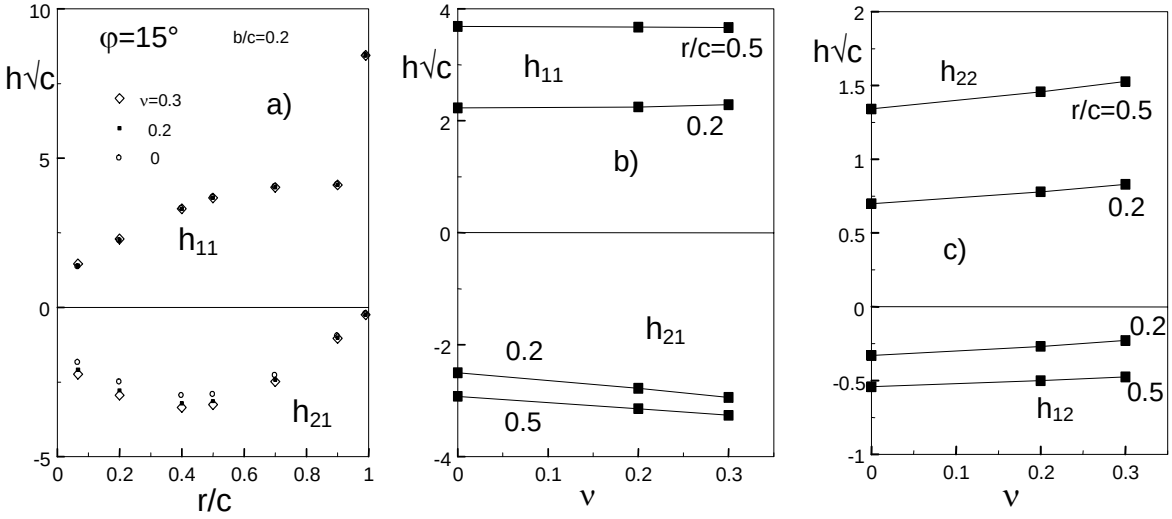

Fig. 31 Influence of Poisson's ratio ν on weight functions for b/c=0.2 and φ=15°.

	A_1	A_2	A_3	A_4	A_5	A_6
$D_1^{(11)}$	18.909	-1.081	.0163	4.970	-.212	.0031
$D_2^{(11)}$	33.132	-2.024	.0329	-7.017	.457	-.0070
$D_3^{(11)}$	-40.096	2.355	-.0373	47.411	-2.916	.0465
$D_1^{(22)}$	7.689	-.422	.0062	.823	.0128	-.0003
$D_2^{(22)}$	-6.249	.516	-.0092	-.366	-.0354	.0014
$D_3^{(22)}$	1.958	-.273	.0059	1.429	.0138	-.0019
$D_1^{(21)}$	-6.409	.332	-.0053	-1.922	.115	-.0017
$D_2^{(21)}$	-55.653	3.249	-.0519	15.347	-.986	.0168
$D_3^{(21)}$	31.798	-1.879	.0302	-32.190	1.902	-.0311
$D_1^{(12)}$	-6.330	.286	-.0043	.660	-.0525	.0012
$D_2^{(12)}$	12.113	-.706	.0112	-5.314	.4066	-.0075
$D_3^{(12)}$	-7.723	.496	-.0079	5.306	-.4064	.0072

Table 9 Coefficients for eq.(74), ν=0.2.

	A_1	A_2	A_3	A_4	A_5	A_6
$D_1^{(11)}$	18.739	-1.072	.0161	5.551	-.2404	.0035
$D_2^{(11)}$	35.404	-2.165	.0353	-10.505	.6799	-.0108
$D_3^{(11)}$	-43.896	2.575	-.0408	57.016	-3.5007	.0560
$D_1^{(22)}$	-6.393	.324	-.0052	-2.014	.1242	-.0018
$D_2^{(22)}$	-56.571	3.289	-.0524	16.889	-1.0552	.0176
$D_3^{(22)}$	30.073	-1.768	.0284	-32.684	1.8973	-.0308
$D_1^{(21)}$	7.858	-.424	.0063	.724	.0155	-.0004
$D_2^{(21)}$	-5.679	.494	-.0089	-.683	-.0228	.0012
$D_3^{(21)}$	1.520	-.257	.0056	1.678	.0036	-.0017
$D_1^{(12)}$	-6.322	.284	-.0041	.675	-.0517	.0011
$D_2^{(12)}$	12.021	-.695	.0110	-5.439	.4078	-.0075
$D_3^{(12)}$	-7.160	.469	-.0076	4.985	-.3894	.0070

Table 10 Coefficients for eq.(74), ν=0.3.

8. Application of the weight functions to cone crack problems

8.1 Hertzian contact stresses

The cone crack extension can be concluded from the condition of K_{II}=0. Loading of a crack by a small mode-II stress intensity factor would result in crack kinking by a small kink angle β

$$\beta \cong -2\frac{K_{II}}{K_I} \tag{76}$$

The new crack turns into the direction for which a disappearing mode-II stress intensity factor exists.

Using the weight functions, eqs.(71a) and (71b), the mixed-mode stress intensity factors K_I and K_{II} of a cone crack were determined for the case of c/a=4 (a= radius of the Hertzian contact zone, Fig. 29c) under Hertzian contact stresses. Due the existence of the mixed weight function terms h_{12} and h_{21}, it is a priori impossible that a cone crack can follow the stress trajectories for a given value of ν.

The resulting mixed-mode ratio K_{II}/K_I as a function of the cone angle and the Poisson's ratio is shown in Fig. 32 by the squares (interpolation of Tables 1-8) and the solid curves (use of eqs.(73) and (76)). The dashed curves were obtained by using the asymptotic weight functions eqs.(68) and (72) exclusively. Whereas the stress intensity factors for the two asymptotic relations differed slightly, the ratio of the stress intensity factors for the two solutions was found

to be identical within the line thicknesses. From the numerical results, it can be concluded that the mode-II stress intensity factor contribution disappears at cone angles of $\varphi \approx 18\text{-}23°$, depending on the special value of ν in the range of $0.15 \le \nu \le 0.25$, whereas application of the asymptotic weight function solutions according to eqs.(68) and (72) yields disappearing mode-II stress intensity factors at clearly larger cone angles (e.g. 33° for ν=0.25 and 37° for ν=0.2). It should be mentioned that the major influence of Poisson's ratio is reflected by the Hertzian stresses which are more strongly influenced by ν than the weight function.

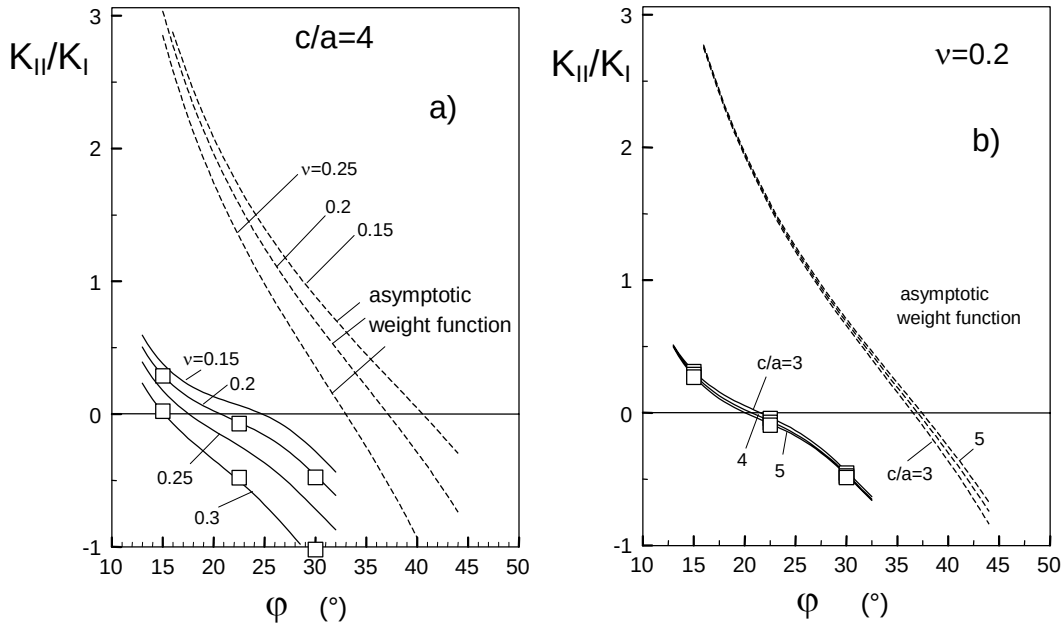

Fig. 32 a) and b) Mixed-mode ratio K_{II}/K_I of cone cracks, computed for sphere loading and several values of ν and c/a. Symbols: application of the full weight function, Tables 1-8, solid curves: eqs.(73) and (74), dashed curves: asymptotic weight functions according to (68) and (72).

8.2 Stresses under a flat stamp

The same computations as for sphere loading were performed for the case of a cone crack introduced by load applied via a flat rigid stamp. The stresses in this case were given by Sneddon [18].

The results obtained with the complete weight function (solid curves: from eqs.(73) and (74), squares: coefficients D from Tables 1-8) and the asymptotic weight functions (dashed curves) are plotted in Fig. 33a. In Fig. 33b the results for sphere and stamp loading are compared. No significant differences between the two different loading types are visible.

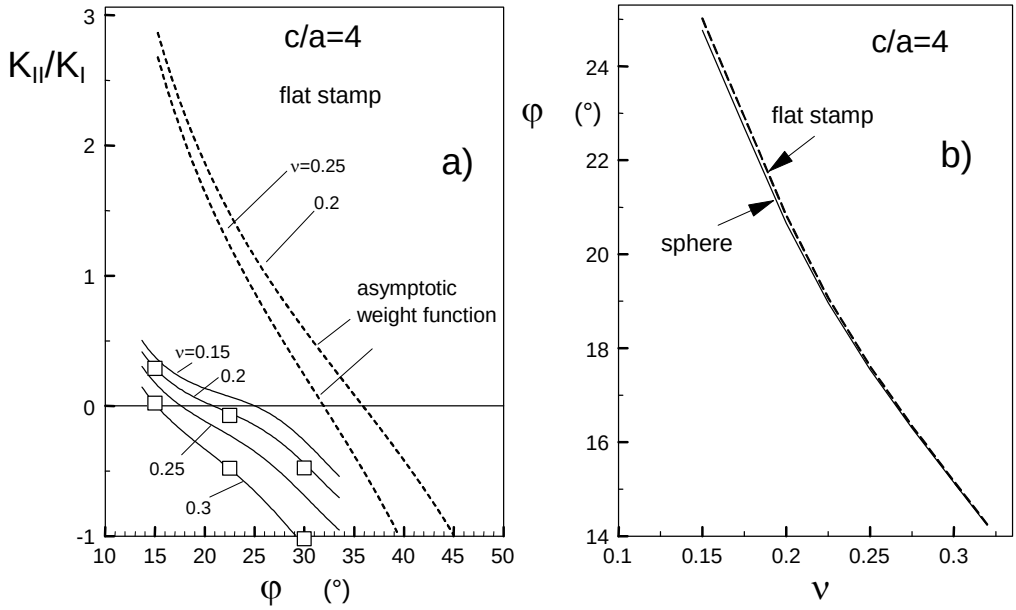

Fig. 33 a) Mixed-mode ratio K_{II}/K_I of cone cracks, computed for stamp loading and several values of ν and c/a=4. Symbols: use of the full weight function, Tables 1-8, solid curves: equations (73) and (74), dashed curves: asymptotic weight functions according to eq.(68) and eq.(72); b) influence of Poisson's ratio on cone crack angles (solid curve: sphere loading, dashed curve: stamp loading).

8.3 Principal effect of a rising crack growth resistance

The computations with respect to cone cracks reported above were performed under the assumption that the stress intensity factor at the crack tip K_{tip}, which governs crack extension and crack deflection, is identical with the applied stress intensity factor K_{appl}, i.e. a material without rising crack resistance curve is considered, for instance glass. In the case of a material with a rising crack resistance curve (R-curve), the effective stress intensity factor K_{tip} is given by

$$K_{tip} = K_{appl} + K_{sh} \tag{77}$$

where the shielding stress intensity factor K_{sh} has the opposite sign of K_{appl} and may be caused by crack face bridging. Such bridging effects will reduce the applied stress intensity factor under both mode-I and mode-II conditions. In the latter case, the crack path condition is obtained as

$$K_{II,tip} = K_{II,appl} + K_{II,sh} = 0 \tag{78}$$

For a material with an R-curve effect, the cone angles must deviate from the value of φ=21° with increasing "strongness" of the shielding effect. In this context it should be mentioned that materials with increasing R-curve behaviour exhibit increasing cone angles. Zeng et al.[19, 20] performed measurements on soda-lime glass, fine-grained alumina and an Al_2O_3/SiC whisker composite. The results were: glass φ≈22°, fine grained Al_2O_3 φ≈26°, and whisker composite φ≈28-31°.

8.4 T-stresses for line loads

Apart from the two stress intensity factor contributions K_I and K_{II}, also the T-stress for the line loads P and Q was determined. It is worth mentioning that under a pure shear load Q also a T-stress occurs. The results are plotted in Fig. 34 and compiled in Tables 11 and 12. Tables 13 and 14 contain the data for ν=0.3.

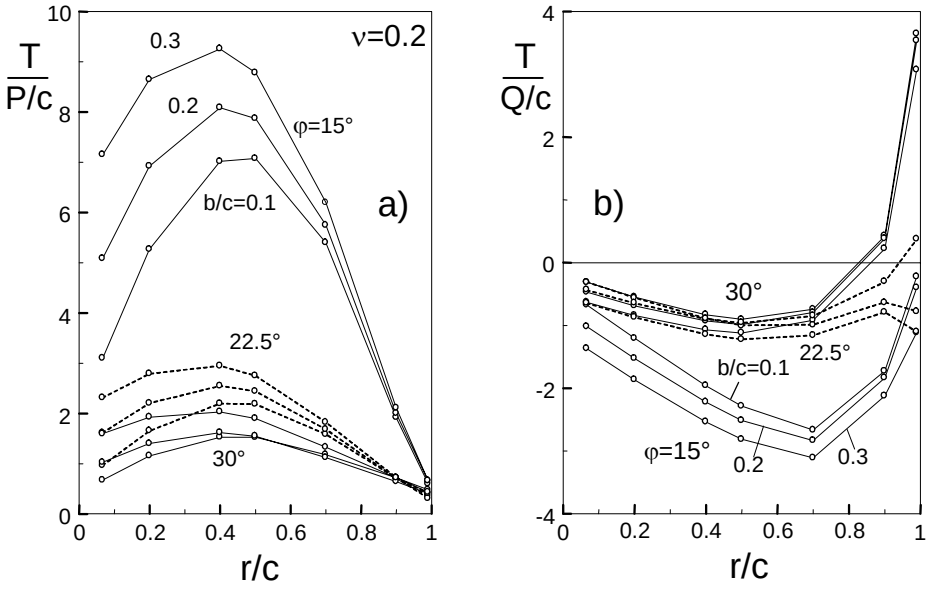

Fig. 34 T-stress for loading by normal (P) and shear (Q) line loads.

φ	x/c	b/c=0.1	0.2	0.3
15°	.0667	3.1037	5.0872	7.1512
	.2000	5.2679	6.9221	8.6446
	.4000	7.0179	8.0884	9.2588
	.5000	7.0762	7.8736	8.7819
	.7000	5.4010	5.7506	6.1992
	.9000	1.9213	2.0022	2.1127
	.9900	.6050	.6633	.6638
22.5°	.0667	.9670	1.6163	2.3132
	.2000	1.6575	2.2053	2.7920
	.4000	2.1977	2.5492	2.9485
	.5000	2.1883	2.4442	2.7514
	.7000	1.5880	1.6834	1.8256
	.9000	.7147	.7066	.7233
	.9900	.4177	.3639	.3119
30°	.0667	.6755	1.0288	1.5982
	.2000	1.1547	1.4023	1.9281
	.4000	1.5301	1.6178	2.0351
	.5000	1.5274	1.5506	1.9014
	.7000	1.1798	1.1228	1.3314
	.9000	.7211	.6457	.7205
	.9900	.4784	.4091	.4355

Table 11 T-stress $T/(P/c)$ caused by line force P (ν=0.2).

φ	x/c	b/c=0.1	0.2	0.3
15°	.0667	-.6697	-1.0176	-1.3688
	.2000	-1.2028	-1.5225	-1.8621
	.4000	-1.9557	-2.2181	-2.5326
	.5000	-2.2830	-2.5136	-2.8146
	.7000	-2.6667	-2.8303	-3.1070
	.9000	-1.7260	-1.8310	-2.1211
	.9900	-.2234	-.3982	-1.1124
22.5°	.0667	-.3081	-.4668	-.6282
	.2000	-.5450	-.6848	-.8376
	.4000	-.8258	-.9292	-1.0666
	.5000	-.9025	-.9877	-1.1187
	.7000	-.7397	-.7920	-.9164
	.9000	.4257	.3853	.2241
	.9900	3.6442	3.5377	3.0720
30°	.0667	-.3115	-.4300	-.6425
	.2000	-.5644	-.6404	-.8697
	.4000	-.8936	-.8891	-1.1419
	.5000	-1.0037	-.9543	-1.2217
	.7000	-.9931	-.8430	-1.1567
	.9000	-.6343	-.2996	-.7867
	.9900	-.7778	.3782	-1.1000

Table 12 T-stress $T/(Q/c)$ caused by line force Q (ν=0.2).

φ	*x*/*c*	*b*/*c*=0.1	0.2	0.3
15°	.0667	3.1749	5.2366	7.3835
	.2000	5.3618	7.0676	8.8470
	.4000	7.0563	8.1525	9.3552
	.5000	7.0629	7.8800	8.8141
	.7000	5.2794	5.6456	6.1136
	.9000	1.7323	1.8305	1.9574
	.9900	.4190	.4936	.5077
22.5°	.0667	.9693	1.6367	2.3560
	.2000	1.6500	2.2090	2.8110
	.4000	2.1434	2.5014	2.9111
	.5000	2.1026	2.3654	2.6824
	.7000	1.4410	1.5468	1.7002
	.9000	.5291	.5357	.5651
	.9900	.2330	.1947	.1527
30°	.0667	.6953	1.0589	1.6541
	.2000	1.1752	1.4222	1.9682
	.4000	1.5174	1.5972	2.0300
	.5000	1.4882	1.5036	1.8691
	.7000	1.0807	1.0207	1.2441
	.9000	.5681	.4987	.5887
	.9900	.3051	.2473	.2879

Table 13 T-stress $T/(P/c)$ caused by line force P (ν=0.3).

φ	x/c	b/c=0.1	0.2	0.3
15°	.0667	-.6697	-1.0176	-1.3688
	.2000	-1.2028	-1.5225	-1.8621
	.4000	-1.9557	-2.2181	-2.5326
	.5000	-2.2830	-2.5136	-2.8146
	.7000	-2.6667	-2.8303	-3.1070
	.9000	-1.7260	-1.8310	-2.1211
	.9900	-.2234	-.3982	-1.1124
22.5°	.0667	-.3081	-.4668	-.6282
	.2000	-.5450	-.6848	-.8376
	.4000	-.8258	-.9292	-1.0666
	.5000	-.9025	-.9877	-1.1187
	.7000	-.7397	-.7920	-.9164
	.9000	.4257	.3853	.2241
	.9900	3.6442	3.5377	3.0720
30°	.0667	-.3115	-.4300	-.6425
	.2000	-.5644	-.6404	-.8697
	.4000	-.8936	-.8891	-1.1419
	.5000	-1.0037	-.9543	-1.2217
	.7000	-.9931	-.8430	-1.1567
	.9000	-.6343	-.2996	-.7867
	.9900	-.7778	.3782	-1.1000

Table 14 T-stress $T/(Q/c)$ caused by line force Q (ν=0.3).

8.5 Stress intensity factors and T-stress under Hertzian contact load

For a Hertzian contact stress of the form

$$p = p_0 \sqrt{1-(x/a)^2} \tag{79}$$

with maximum pressure p_0 in the centre (Fig. 35) and $a=b\cos\varphi$ (see Fig. 29), the mixed-mode stress intensity factors and the T-stress term were determined with the FE method. The K results are plotted in Fig. 36 and compiled in Table 15. The stress intensity factors are expressed by the geometric functions F_{I} and F_{II} as

$$K_{I,II} = p_0 F_{I,II} \sqrt{c} \tag{80}$$

The T-stress is illustrated in Fig. 37 and compiled in Table 16.

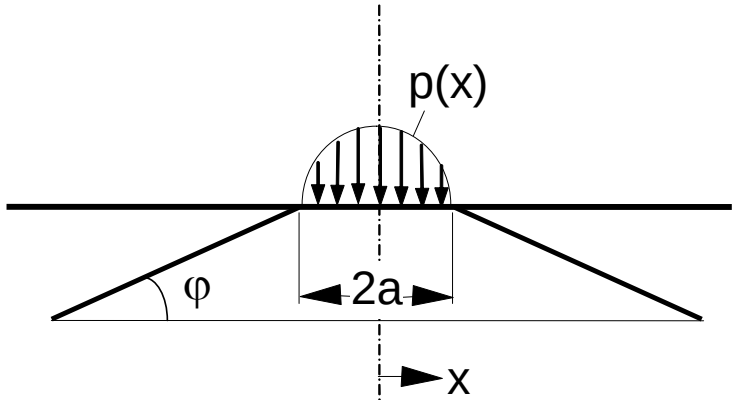

Fig. 35 Cone crack under Hertzian contact pressure.

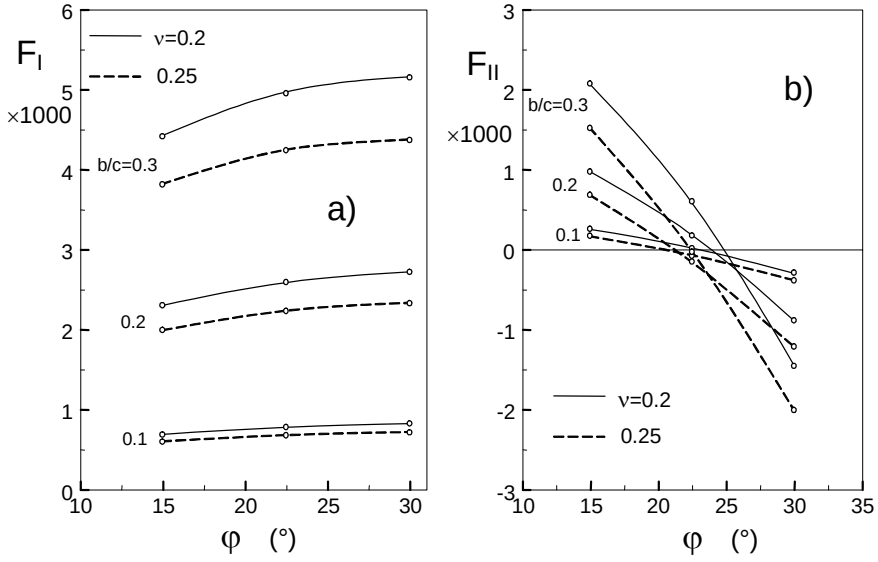

Fig. 36 Geometric functions for mixed-mode stress intensity factors.

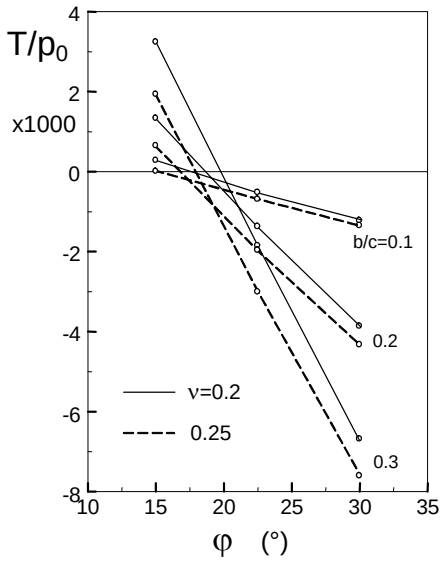

Fig. 37 T-stress of the cone crack under Hertzian pressure.

φ	*b*/*c*	1000×F_{I}	1000×F_{II}
15°	0.1	0.6849	0.2559
	0.2	2.300	0.9710
	0.3	4.411	2.073
22.5°	0.1	0.7772	0.0140
	0.2	2.590	0.1721
	0.3	4.951	0.6005
30°	0.1	0.8230	-0.2922
	0.2	2.718	-0.8889
	0.3	5.150	-1.460

Table 15 Geometric functions for stress intensity factors (ν=0.2).

φ	ν	*b*/*c*=0.1	0.2	0.3
15°	0.2	0.2803	1.3323	3.2393
	0.25	0.0793	0.6473	1.9297
	0.3	-0.1201	-0.0342	0.6243
22.5°	0.2	-0.5219	-1.3724	-1.8542
	0.25	-0.6941	-1.9675	-3.0105
	0.3	-0.8604	-2.5444	-4.1349
30°	0.2	-1.2249	-3.8657	-6.6901
	0.25	-1.3550	-4.3300	-7.6051
	0.3	-1.4761	-4.7655	-8.4679

Table 16 Normalised T-stress as 1000×T/p_0.

References

[1] Fett, T., Computation of the crack opening displacements for Vickers indentation cracks, Report FZKA 6757, Forschungszentrum Karlsruhe, Karlsruhe, August 2002.

[2] Hill, R., Mathematical Theory of Plasticity, Oxford University Press, 1950, Oxford.

[3] Rödel, J., Rissüberbrückung in keramischen Werkstoffen, VDI-Verlag, Reihe 5: Grund- und Werkstoffe, Nr. 331, Düsseldorf 1993.

[4] Evans, A.G., Charles, E.A., Fracture toughness determinations by indentation, J. Am. Ceram. Soc. **59**(1976), 371–372.

[5] Fett, T., Kounga, A. B., Rödel, J., Crack opening displacements of Vickers indentation cracks, to be submitted to Acta mater.

[6] Kocer, C., Collins, R.E., Measurement of very slow crack growth in glass, J. Amer. Ceram. Soc. **84**(2001), 2585-93.

[7] Leevers, P.S., Radon, J.C., Inherent stress biaxiality in various fracture specimen geometries, Int. J. Fract. **19**(1982), 311-325.

[8] Cotterell, B. and Rice, J.R., Slightly curved or kinked cracks, International Journal of Fracture **16**(1980), 155-169.

[9] Kocer, C., Collins, R.E., The angle of Hertzian cone cracks, J. Amer. Ceram. Soc. **81**(1998), 1736-42

[10] Roesler, F.C., Brittle fractures near equilibrium, Proc. Phys. Soc. London, **B69**(1956), 981-92.

[11] Lawn, B. and Wilshaw, T.R. Fracture of Brittle Solids, Cambridge University Press (1975).

[12] Frank, F.C., Lawn, B.R., On the theory of Hertzian fracture, Proc. R. Soc. London, **A299**(1967), 291-306.

[13] Lawn, B., Wilshaw, T.R., Hartley, N.E.W., A computer simulation study of Hertzian cone crack growth, Int. J. Fract. **10**(1974), 1-16.

[14] Mouginot, R., Maugis, D., Fracture indentation beneath flat and spherical punches, J. Mater. Sci. **20**(1985), 4354-76.

[15] Fischer-Cripps, A.C., Predicting Hertzian fracture, J. Mater. Sci. **32**(1997), 1277-1285.

[16] Fett, T., Munz, D. (1997) Stress Intensity Factors and Weight Functions, Computational Mechanics Publications, Southampton, UK.

[17] Huber, M.T., Zur Theorie der Berührung fester elastischer Körper, Ann. Phys, **43**(1904), 153-63.

[18] Sneddon, I.N., Boussinesq's problem for a flat-ended cylinder, Proc. Cambridge Phil. Soc. **42**(1946), 29.

[19] Zeng, K., Breeder, K., Rowcliffe, D.J., The Hertzian stress field and formation of cone cracks – I. Theoretical approach, Acta Metall. Mater. 40(1992), 2595-2600.

[20] Zeng, K., Breeder, K., Rowcliffe, D.J., The Hertzian stress field and formation of cone cracks – II. Determination of fracture toughness, Acta Metall. Mater. 40(1992), 2601-2605.